University of Stavanger

FACULTY OF SCIENCE AND TECHNOLOGY

MASTER'S THESIS

Study programme/Specialization: **Engineering Structures and Material Science/ Specialization in Renewable Energy**	Spring, 2020 Open / ~~Confidential~~
Author: **Owolabi, Jibola Obafemi**	

Programme coordinator:
     Dimitrios Pavlou
 	
Supervisor(s):
     Dr. Knut Erik T. Giljarhus	

Title of master's thesis: **FULLY RESOLVED CFD SIMULATION OF A TIDAL STREAM TURBINE IN BI-DIRECTIONAL DUCT**	
Credits (ECT): 30	
Keywords: **BEMT, AMI, CFD, OpenFOAM, Torque, Power Coefficient, Bi-Directional Duct, Open Water Characteristics, Pitch Angle**	Number of pages: + supplemental material/other: Stavanger, 29th June, 2020

Title page for master's thesis
Faculty of Science and Technology

University of
Stavanger
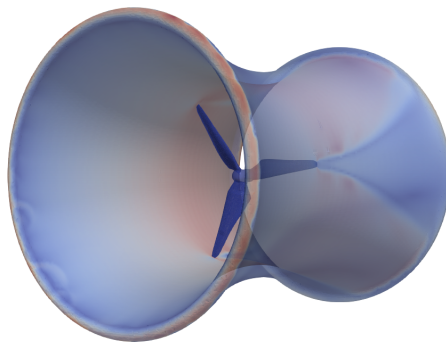
MSc ENGINEERING STRUCTURES AND MATERIALS

MASTER THESIS

Fully Resolved CFD Simulation of a Tidal Stream Turbine in Bi-Directional Ducted

AUTHOR:

Owolabi, Jibola Obafemi

Abstract

Renewable energy, in it's present contribution, is inadequate to meet up with the global energy demand. Though the Tidal current energy is known for its inherent great potential, its impact in the world's total renewable energy is low, hence it is pertinent to study one of the key component of the tidal energy system - the turbine blade.

In this report the performance of a propeller was predicted using BEMT technique and the importance of this theory in the comprehension of an efficient propeller blade in relation to increasing incoming flow velocity on the propeller is discussed. This research study presents the results obtained from the investigation of the flow over an open center high solidity tidal propeller obtained from Framo AS through the use of openFoam as a CFD tool. It also investigated the flow over a BEMT designed turbine blade generated from Qblade which serves as an engineering computational method for the simulation of aerodynamic loads on rotor blades as well as it's analytical derivations.

In order to meet up with the increased accuracy as a result of complications related to turbine blade design, it was important to consider using the BEMT technique to generate the turbine blade for the simulation. Afterwards, the simulation analysis was performed for each foils that makes up the MHKF turbine blade and for the Framo AS propeller free stream analysis. From the CFD analysis of the open center turbine, the pitch towards the blade root has a high angle of attack at a low TSR resulting in separation of flow at the foil trailing edge which probably contributed to the low efficiency obtained from the simulation analysis. Also, for the MHKF1-180s, 240s and 400 hydrofoils (in order of blade tip to blade root position), their optimum angle of attack amounts to be 15.5 degrees, 11.5 degrees and 10 degrees respectively as obtained from the CFD simulation.

Conclusively, the CFD analysis of the Framo propeller in free stream shows that the pitch of the blades should probably be reduced towards the root in order to give an overall optimal flow at a higher TSR. It also shows that the maximum Cp (0.28) is a moderate efficiency for the turbine. Also, the BEMT generated 3-bladed turbine efficiency at flow velocity of 5m/s has a power coefficient of 0.4 at TSR of 4 which is also a little lower compared to the validation case efficiency of 0.45 at the same TSR of 4.

Keywords: CFD, OpenFOAM, AMI, Laminar and Turbulent flow, Open center turbine, Duct design, BEMT, Pitch angle.

Preface

This thesis was written at the Faculty of science and technology, University of Stavanger in partial fulfillment for a Master of science degree in Mechanical and Structural Engineering and Material Science.

To the creator of the universe. To mum and Dad, thank you for everything. Also to my professor, Knut Erik, thank you for the patience and guidance all through.

Table of Contents

List of Tables

List of Figures

Abbreviations

CAD	=	Computer Aided Design
CFD	=	Computational Fluid Dynamics
RANS	=	Reynolds Average Number
MHKF	=	Marine Hydro Kinetic Foil
stl	=	StereoLiThography
CAE	=	Computer-aided engineering
BEMT	=	Blade Element Momentum Theory
BEM	=	Blade Element Method
IEA	=	International Energy Agency
Co	=	Courant number
MRF	=	Moving Reference Frame
AMI	=	Abitrary Mesh Interface
y+	=	yPlus
Cp	=	Power Coefficient

Chapter 1

Introduction

1.1   Project Background

The need for the development of more energy sources has been globally triggered mainly by two factors. The first being the alarming escalation in the trend the global population size which according to the world population prospect in 2019 was 7.7 billion, with an increase of 1 billion over the course of 12 years since 2007 and 2 billion increase since 1994 [28]. Also, the International Energy Agency report in 2018 reported an increase in the energy demand globally by 2.3 percent, an enormous amount which was contributed by the consumption of fossil fuels resulting to a 1.7 percent increase in the emission of CO_2. Which brings us to the global negative effect our reliance on fossil fuel is stimulating which is the second factor motivating the diversification of energy reliance to sustainable and renewable energy sources.

Although renewable energy industries are developing, its present contribution is inadequate enough to tackle the increasing global energy demand. This is largely due to shortcomings in the areas of cost effectiveness and increased reliability in energy production. However, in the quest for a sustainable and renewable future, the challenge of having various unreliable, short-lived and the potentially negative environmental impacts inherently characterized by these energy sources has made it pertinent for more research and analysis of another option of renewable energy source which must be reputable, highly predictable and most of all, be uninterrupted. It is simple arithmetic to say that in order to increase energy supply to meet the market demand, energy produced must be increased. This results in making undeterred attempts at identifying, mastering and understanding the process of harnessing reliable energy from nature, thereby, minimizing our dependence on fossil fuel generated energy and ultimately trimming down emissions and environmental hazards.

It is however worth noting that the energy generated from renewable sources even though has a few demerits when compared with fossil fuel generated energy, there are still a lot of potential merits related to exploiting these sources. As a result of the prolonged delay in providing a lasting solution to these shortcomings caused by fossil fuel

exploitation, more negative impacts on the environment like extreme rise in temperature and global warming leading to wildfire storms, rise in sea level resulting in flooding, harsh changes in weather and climatic conditions globally, extreme change in pattern of wind circulation and most of all, enormous loss of wildlife should be expected. Evidently, recent trends associated with these predictions were the wild firestorm in Australia with a record temperature increase prior to this event, a series of hurricanes that hit the United States of America in recent times ranging from hurricane Katrina to Irma, to hurricane Dorian, Florence and a list of others.

One major challenge to the generation of energy from promising renewable sources is the predictability for consistent and uninterrupted power production. The ocean has however proved over time to be a reliable option to be identified with for various human exploitation, most of all, energy demand in this case which is the most pressing and demanding issue facing humanity at this dispensation. Moreover, an insight into the naturally backed theory behind the reliability of this renewable energy source has made harnessing tidal current energy more cognizant in the renewable energy industry and has inevitably made the study and exploitation of this energy source more cost effective thereby commercializing this energy source and ultimately making it available for end users at the lowest price possible. This however cannot be achieved without critiquing every process involved in the energy generation from the ocean and utilizing the knowledge we as human has acquired over time to conquer the challenges faced in this potentially advantageous and paramount plight.

Unlike most energy sources, understanding the concept of tidal waves and current which originates from the gravitational and centrifugal forces of the moon, sun and the earth needs to be explicitly clarified. Meanwhile, this can be effectively relayed by utilizing visual aid in order to study, evaluate and access the genesis of this phenomenon. As stated by A. Owen, *"The moon is responsible for the largest proportion of the tidal forces applied to the earth, but it is not independent in its influence, since not only does the sun also affect the tidal forces, but the moon's own tidal influence is modified by the sun's gravitational field. These cycles are themselves modified by the effective influence of the sun, and occasionally other planets within our solar system, depending on their relative positions"* [31]. The universe as opposed to our reality is connected one way or another. Everything on the surface of the earth experiences gravitational force which literally is the attractive force that all matter exerts on other matter, and this is the basic principle that confines us to the surface of the Earth. In order to explain the relationship between the tidal current, the moon and the sun, it is important to know why a ball thrown vertically upward falls towards the earth or why we as human are not floating in the atmosphere. Centered on our knowledge on the universal law of gravitational force, both the earth and the ball contribute a mutual and equal force to attract each other to itself. But then, Newton's second law states that the force applied is the product of mass and acceleration. This makes the acceleration to be inversely proportional to the mass, thereby explaining the reason behind the fast acceleration of the ball towards the surface of the earth as the mass of the earth is immensely greater than the mass of the ball which also explains what holds the everything that makes up the earth together. However, the moon also exerts its own gravitational force which influences some compositions that makes up the earth which in this case will be the tide that we are studying. Now, let's imagine as shown below that the

moon is directly in line with the earth or directly above it, there is an exertion of gravitational force between these two which results in the rise and fall of the tides as a function of the location on earth that is of proximity to the moon.
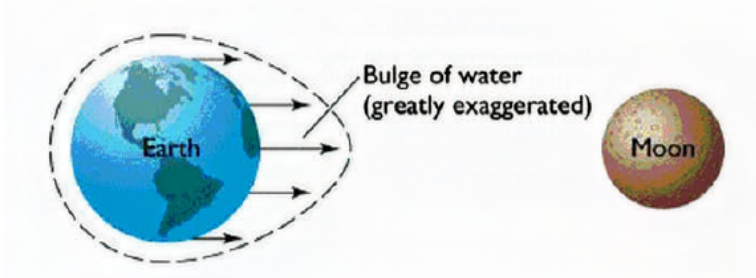
Figure 1.1: Effect of the moon gravitational force on the earth [34]

As we know, the position of the moon with respect to the earth as it rotates varies, it is however important to also note that the opposite side of the earth relative to the position of the moon at any time also experiences the bulge or rise of the ocean but in the other direction as shown in Figure 2 below. This is largely because of centrifugal force as a result of the rotary movement of the earth.
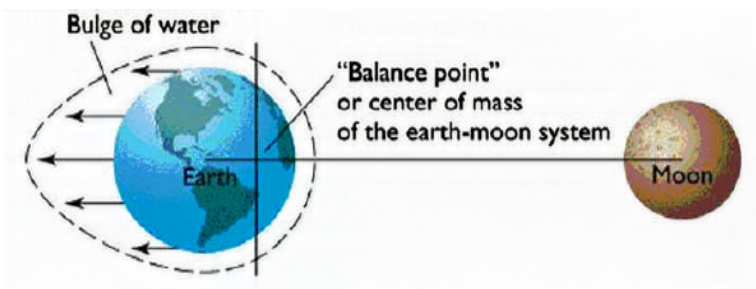
Figure 1.2: Centrifugal force effect on the earth's side relative to the moon [34].

According to NASA, the Moon completes its orbit around Earth in 27 Earth days. But as a result of the Earth's movement as well, the Moon appears to orbit us every 29 days. This effect of the gravitational force exerted by the moon on earth results in the rise and fall of the ocean, completely dependent on the position of the moon relative to the earth.
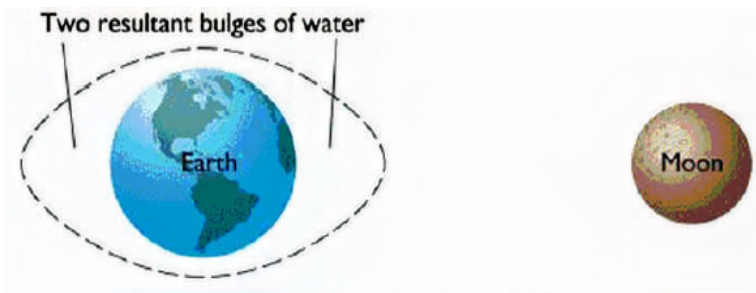
Figure 1.3: Ocean current upsurge in relation to the moon's position [34].

Meanwhile, the influence of the sun on the rise and fall of the tide either intensifies or lessen the effect of the moon's gravitational force on Earth as shown in Figure 4 below. When the position of the sun is relative or parallel to the moon, the bulge in tide will be escalated as the sun increases the moon's gravitational force. However, when the sun is in a perpendicular state or at right angle with the moon, there is a drastic reduction in the tide level as the moon's gravitational force will be highly rendered insufficient or incapable to effect a bulging influence on the tide.
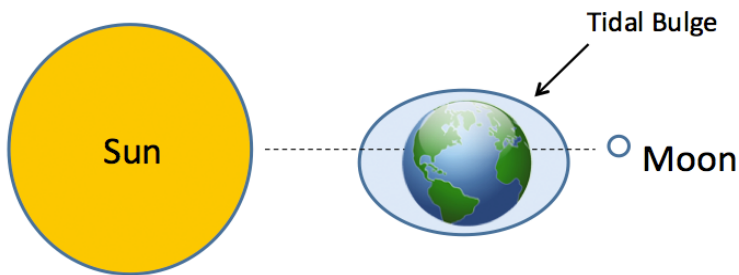
Figure 1.4: Effect of the sun in a parallel position relative to the moon [12].
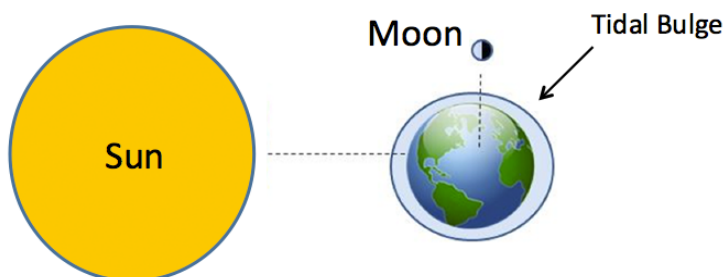
Figure 1.5: Effect of the sun in a perpendicular position relative to the moon [12].

Interestingly, harnessing power from the kinetic energy of the tide does come with its own challenges and these reinforce the need for further research. Most of these challenges are preconceived potential disadvantages such as environmental effect on the mobility and migration of marine animals resulting to a more serious responsibility as plant constructions covering a large area will pose serious threat to the existence of marine life. Also, as a result of the new technology and early phase of this industry, it is still cost intensive.

With an head start of being an energy source with minimal adverse effect on the environment, the question to ask then is, to what end does performing a computational fluid dynamics simulation of a tidal turbine be of help in achieving the aim of cost effectiveness, performance prediction, possibility of analysis at varying parameters and comprehension of flow reaction at different situations which will result in the optimal utilization of this energy source's potential. In other words, the efficient working mechanism of tidal turbine is solely based and reliant on the manipulation of the tidal current kinetic energy which causes the rotational motion of tidal turbine rotor, highly influenced by the movement of water across the blades which are positioned at an orientation that fully takes advantage of the kinetic energy of the moving water and also, skillful mastery of the interaction of the turbine blade airfoil profile design in order to efficiently generate torque. This however, reiterates the importance of utilizing CFD simulation to effectively analyze varying work conditions (for example, exploitation of weaker tidal current) and different models of energy converting devices in order to invent or develop existing designs so as to understand the dynamics of the fluid and take advantage of this knowledge to orchestrate efficiency of the tidal turbine operation which for this purpose, CFD simulations will be utilized due to the low cost it offers.

1.1.1   Scope/Objective of this project

This project is an improvement on a research work which evaluates the performance of an actuator disc (which is a simplified representation of a tidal turbine) by introducing a Bi directional flow enhancing Duct [16], (as a result of the Duct's ability to boost velocity limitations, thereby improving efficiency). This present study work is limited to;

1. Validation and efficiency comparison of an experimental case set up by a pump manufacturing company called Framo AS and the CFD analysis of the same case set up will be carried out using openFoam as the CFD tool in this research work. Then an analysis of ducted turbine case in order to analyze the effect of the aerodynamically designed duct in the performance of the propeller will be investigated and compared with the analysis in free stream.

2. With the implementation of BEMT method, the twist toward the tip of a turbine blade is achieved making use of the MHKF1-180, 240s and 400 foil profiles which were recently developed for use in fluid of higher density like water. These foil profiles will also be analysed to visualize the dynamics of flow in relation to lift and drag generated. Then this blade will be developed into a low solidity 3 bladed horizontal turbine and validated with a similar research work on a 1:8.7 scale [6], in order to compare flow analysis in free stream and Bi directional flow enhancing Duct.

1.1.2 Project Outline

The study outline includes:

1. Chapter One: Introduction to the research work.

2. Chapter Two: Background study on the history of tide exploration and Literature review on ducted design for tidal stream turbines.

3. Chapter Three: Theory

4. Chapter Four: Methodology on the Framo AS Propeller case

5. Chapter Five: Methodology on the MHKF Turbine.

6. Chapter Six: Results and Discussion of the research work carried out will be diligently examined.

7. Chapter Seven: Conclusion on what has been studied and Recommendation on future work.

Chapter 2

Literature Review

2.1 Early History of Tidal research

The importance of energy in a modern society cannot be over emphasized and this has initiated at different levels several researches over the years. These researches started from the exploration of fossil fuels, followed subsequently by researches against the increasing adverse environmental impacts taking effect globally, which prompted an urgent diversion into research and technological development to harness energy from nature which presents less danger to our environment. However, harnessing energy from the ocean although has been in application for quite sometime now and there has not been lack in proposals for tidal current energy conversion systems, but a lot of them are complicated, financially on the high side and most of all unverified [30].

During the last few decades, our knowledge of Roman watermills has increased at such a rate that historians of technology had tried to revise their understanding of the part water-power played in Roman industry [33]. Moreover, our archaeological knowledge over the years has also given us an overview of the Roman Empire ancient works to shine more light on the practical utilization of ocean current to generate power in corn milling, mining, shipping and bath installations by the first century AD [33]. Furthermore, we know the Romans had a good understanding of tides evident from the writings of Strabo115 (64 BC to 21 AD) and Pliny the Elder (23 to 79 AD) [33]. Their accounts revealed knowledge of diurnal and monthly tides, and the equinoctial/solstitial inequality that cause the springs to reach their highest levels around the equinoxes twice each year [33]. However, this study could not present if the Roman knowledge of the ocean tides yielded an alternative source of water power. More importantly, the design and the operational details of the Roman water wheel although not accurate, is worth noting as these concepts can be imitated, replicated and built upon if challenges relating to working mechanism of the modern turbine blade is encountered.

2.2   Global environmental impact

A tidal power scheme is a long-term source of electricity. Although, this is a measure towards the reduction of local and global green house emission, however, the process involved from the manufacturing to decommissioning at the end of it's life cycle has to be reviewed in order to accurately propose the viability of this energy extraction system. Mainly with regard to tidal barrage, J. Wolf et al reviewed the possible negative impacts extraction of tidal power would have on the environment at large [43]. Exploration of environmental changes ranging from physical changes at close proximity around the energy conversion structure like scouring and possible marine life habitation loss to larger impact as a result of potential interference during construction, net reduction in saline level and contaminated water quality was considered to be inevitable [43]. However, it has been stated that if a proposal for the Severn Barrage can be built, it is predicted to save 18 million tonnes of coal annually [39]. If reliance on fossil fuel resources drops during the 21st century, as projected by Hubbert peak theory, tidal power is one of the viable source of energy prospects to be developed in order to meet the emerging energy demand [18]. This positive effect of operating tidal power devices will greatly decrease the output of greenhouse gases into the atmosphere when compared with other demerits associated with this energy source converter. Moreso, investigative research to combat other challenges will be further developed and incorporated.

2.3   Tide Study and Improvements in Modern Society

In our world today, the need for exploration and aim to attain excellence with the generation of energy from the ocean is inspired by the level of deep water knowledge and offshore domination experienced in the oil and gas industry and most recently the wind turbine industry. Additionally, another motivation according to the IEA is to reduce emissions from oil and gas operations, thereby serving as a crucial measure in helping countries to get environmental gains from using less emission-intensive fuels and also industrial clean energy transitions [19]. Going offshore, Wind Turbine farms are the most similar to turbine farms harnessing energy from the tides, both in structure and mode of operation. Horizontal or vertical axis turbines are placed in the flow in such a way as to minimize interference and be exposed to the largest currents. It is however imperative to note that all these transformations in Wind Turbines up on to tidal turbines are direct technology transferred from the oil and gas industry which according to IEA would be more difficult, challenging and more expensive without the oil and gas industry [19].

As it is in other European countries and around the world, Denmark's clean energy transition experience bears testimony to the potential of environmentally sustainable growth: addressing climate change while enabling the economy to expand [19]. After the oil crisis in the year 1973, Denmark began to explore the possibilities energy generation from the wind. The first commercial wind turbine was erected in 1979, and from a developing wind turbine industry emerged a country generating 30 percent of all energy used from renewable sources [29]. As a result of the present global confinement, various sources of pollution has been put on hold making the decline in the carbon dioxide emission equally rubbing off positively on the environment. However, it is a ticking bomb ready to go off

once all activities are back to normal. The vision and strategy to remarkably curtail the resurgence of this apparently impending menace aiming for catastrophe is to intentionally impose a continuous reduction to the already plummeting rate of emission [19]. Therefore, there is no better time than now for governments around the world to invest into the renewable energy sector and consider the vital role this sector would play in getting the economy back in shape, also with the benefit of attaining totally reduced emissions. However, in recent times, more support has being falling in line with the development of energy generation from the tidal current with the aid of a turbine, attaining optimal performance has been one major problem faced among numerous ones in the utilization of this energy conversion device ranging from manufacturing to power storage.

2.4 Review on ducted tidal stream turbines

As a promising and reliable energy source coupled with the early maturity phase of this energy generation source, various research analysis has been carried out on ways to effect efficiency on the performance of the tidal turbine over the years. Several studies has been carried out for enhancing the performance of tidal current turbines either by analytical, experimental and numerical techniques, however, ducted propellers happens to be one of the unconventional attachment systems mostly utilized to achieve a higher propulsion performances.

A Duct which is also referred to as a Diffuser can be described as a device placed around the circumference of a turbine rotor with the aim of increasing the mass of flow through the rotor swept area thereby, increasing turbine efficiency [26]. These designs are in different shapes and as a result of this, there are varieties of ducts designed to take advantage of their individual different physical principles to further accelerate or decelerate fluid flow. The duct aerodynamic geometry is developed from an airfoil as a result of its aerodynamic curvature and this provides numerous benefits for the tidal turbine, some of which includes blades protection, aligning flow towards the rotor and also support for the load the turbine imposes [15]. Various geometry of duct designs will be examined in this section to determine how these geometries affect the performance of the tidal turbine in respect to the power and efficiency generated. In order to overcome the low efficiency challenges associated with current tidal turbines, there is an urgent need to establish an efficient measure to improve on it's performance, thereby, the introduction of aerodynamically efficient ducts whose inflow tract and smooth transition of flow aids the rotational operation of propeller blades designed for the tidal stream turbines. According to Koh et al [22], who carried out a research study on the effect of Propulsion Performance on a Malaysian fishing boat with ducted Propeller and stressed on the efficiency derived from its application, as a result of now been extensively utilized in ships [22].

Ducts are generally classified into Bi-directional and Uni-directional. Bi-directional duct increases flow towards the turbine by directing flow towards the airfoil in a way to maximize both the incoming flow and the ebb of the tidal current flow for efficient power production [16]. While Uni-directional ducts on the other hand takes advantage of the incoming flow and direct it towards the rotor for optimal efficiency.
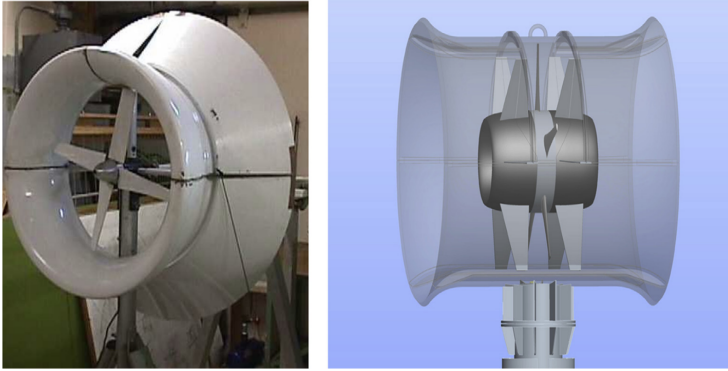
Figure 2.1: Ducted turbine Models (Uni-directional duct [14] on the left and Bi-directional duct [9] on the right)

In a preliminary study based on a research analysis that aims at analyzing the effect of positioning a tidal turbine in a bi-directional duct, with the intent of introducing the duct is to accelerate the incoming flow, thereby increasing the power output of the turbine as both the ebb and the flow of the tidal flow can be exploited for power production in a bi-directional duct, a 50 percent increase in the efficiency of the ducted actuator disc was recorded against the bare turbine in free stream [16]. Moreover, the duct design used for analysis in this research was obtained from Giljarhus, [16] which is a developed model from a previous research work where an actuator disc was used in place of a turbine.
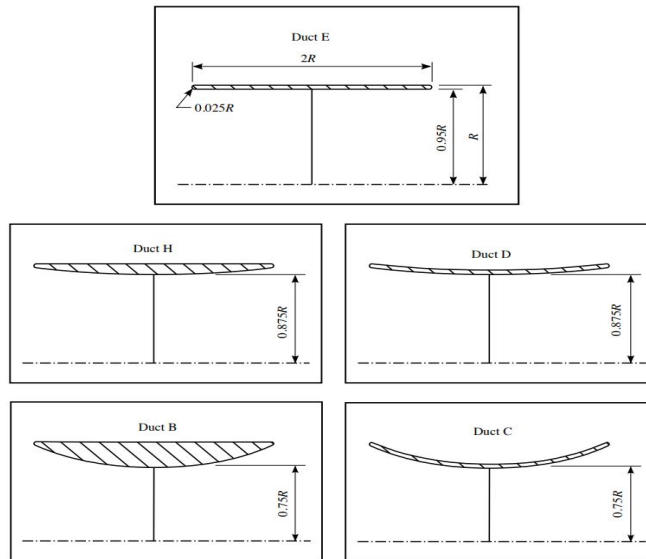
Figure 2.2: Profiles of ducts tested in parametric study (where R is radius) [15]

The duct geometry design which was originally used in the evaluation of ducted tidal turbines in relation to unducted turbines using Reynolds-averaged Navier-Stokes solver ANSYS Fluent to examine the effects of the duct's camber and thickness where all ducts considered were created from circular arcs and represents a settlement between simplicity of design and manufacture, most importantly, the significance of hydrodynamics factor [15]. Likewise, an actuator disc was used in the representation of the turbine rotor as it depicts the thrust and generates optimal energy, making it a viable alternative to a rotor in the analysis of the effect of duct geometries, although it doesn't take into effect the losses due to centre body, the blades and turbulence [15].However, this study also evaluates the effect of duct camber on the power extraction by correlating ducts C,D and E as shown in Fig 2.1 at optimal operating points of K = 2, 1 and 0.5 respectively [15]. It was however observed that there are contrasts in power coefficient as a result of the velocity an the area of the actuator disc, thereby, bringing about similar disc pressure changes for each device. Whereas, Duct C which is the most cambered device generates the highest velocity through the actuator disc, however, at a reduced disc area. Duct E, does not achieve flow acceleration, as a result, generates the lowest power coefficient. Finally, the study reported Duct D achieved the conformity required between the flow acceleration and power-extracting area indicating that a moderate degree of camber is preferable. Also, to support it's claim that camber ducts can support high drop in pressure and generate more power compared to uncambered ducts, it was observed that Duct C and D permits low static pressure at their exits, prompting greater wake expansion at the downstream [15]. The study however, having shown that a fair measure of camber is recommended to facilitate an increased velocity of flow towards the disc in order to count for the reduced disc area, reported an increase in the power density which is the rotor based power coefficient, but a reduction in the power extraction as a result of the limit the duct imposed on the downstream flow expansion, where power coefficient was in relation to the frontal area of the device, a power coefficient of 0.85 was generated by an unducted disc while a ducted disc generated a power coefficient of 0.5 [15].

To achieve an accurate design of a turbine blade, there are different approach that can be undertaken, one of which is the Blade Element Method due to it's accuracy and reliability over time. Orignally, the wind turbine blade design technique experience was acquired from the aircraft industry. However, as a result of the working conditions and the complicated flow in which turbine blades operates in, most of the concepts in this method are not directly applicable to a wind or tidal turbine [24]. In the optimization of turbine, although BEM is well recognized in the wind turbine industry, application of this tool for the optimization of tidal turbine can be of great value in terms of improving the efficiency of tidal turbine power generation. In a similar study, the design and analysis of tidal turbine using BEM with CFD was reviewed. It was reported in this research how BEM can be applied to conventional turbines but inapplicable to ducts as the accepted BEM equation represented by the stability between axial momentum and force is not realistic for turbines with ducts as a result of the duct's interference with the flow [37]. However, the study explained the use of a procedure whereby the effect of the duct can be taken into account in relation to efficiency and power coefficient, thereby, making it possible to introduce BEMT for ducted turbines [37].

Chapter 3

Theory

3.1 Governing Equations

3.1.1 Bernoulli Principle

Bernoulli's equation is one of the fundamental theory in fluid mechanics. Although it is based on the incompressible ideal fluid, on the basis of stationary flow, but when a lot of fluid flow can be approximately regarded as ideal fluid, using Bernoulli equation can get many useful conclusions [35]. Basically, Bernoulli's principle deals with the conservation of kinetic, potential and flow of energy of fluid stream and the conversion of these in flow regions where viscous forces are negligible [44]. Most importantly, the properties and flow of the fluid dynamics can best be illustrated by the fundamental governing equations; Mass conservation, Momentum conservation and Energy conservation. Bernoulli's principle can be mathematically represented by;

$$\frac{P_1}{\rho} + \frac{V_1^2}{2g} + Z_1 + h_p - h_f = \frac{P_2}{\rho} + \frac{V_2^2}{2g} + Z_2 \tag{3.1}$$

where; h_p is the Compressor head, h_f is the Frictional head.

In the derivation of Bernoulli equation for incompressible flow, an approximation used is that ρ = constant. In order to fulfill this condition in liquid and gases, Mach numbers are less than 0.3 [44].

In regard to this project, the fundamental explanations will be given to the two theories responsible for lift of the hydrofoil; the Bernoulli's equation and the Euler's equation. The importance of the equation of motion cannot be over emphasized either for a system or for a control volume. Solution using the control volume in fluid dynamics is more proficient than the approach of using the system which is the definite mass of the fluid [38]. However, the basic laws governing the physics of continuous materials can only be applied to the system which therefore gives the need for the establishment of a relationship known as the reynolds transport theorem which basically describes the connection between the system

and the control volume. This gives;

$$\frac{dN}{dt} = \frac{d}{dt}\int_{andV_{(system)}} = \int_{V_{cv}}(\rho\beta)\,dV + \int_{S}(\rho\beta)\mathbf{u}\cdot d\mathbf{S} \tag{3.2}$$

where;

$V_{(system)}$ is the system volume,V_{cv} is the control volume, rho is the density of fluid, u is the velocity, S is the control surface, $beta$ is the change in fluid properties in relation to mass $\frac{dN}{dm}$, N is fluid properties like mass, energy or momentum, m is the mass, S is the control surface.

The Reynolds transport theorem literally describes the system change in a control volume as a function of the inflow and outflow through the control volume taking into account the changes while in the control volume. To put in perspective, lets consider a pool as a fixed control volume, there is a change in the quantity of water in the pool if the inflow and outflow are not equal [38]. Since the mass of a system does not change, the Reynolds transport theorem can then be defined as;

$$\frac{dN}{dt} = \frac{d}{dt}\int_{V_{(system)}}(\rho\beta)\,dV = \int_{V}\frac{\partial(\rho\beta)}{\partial t}\,dV + \int_{S}\rho\beta u_i n_i\,dS \tag{3.3}$$

Therefore, the Reynolds transport theorem can as well be written as

$$\frac{dN}{dt} = \int_{V}[\frac{\partial(\rho\beta)}{\partial t} + \frac{\partial(\rho\beta u_i)}{\partial x_i}]dV \tag{3.4}$$

3.1.2   Euler Equation

Continuity equation for incompressible fluid;

$$\frac{\partial u_i}{\partial x_i} = 0 \tag{3.5}$$

Momentum Equation;

$$\rho\frac{\partial u_i}{\partial x_j} + \rho\frac{\partial(u_i u_j)}{\partial x_j}] = \frac{\partial P}{\partial x_i} + \eta(\frac{\partial^2 u_i}{\partial x_j^2} + \frac{\partial^2 u_j}{\partial x_j \partial x_i}) + S_{M,i} \tag{3.6}$$

Therefore, for incompressible flow,

$$\frac{\partial u_i}{\partial t} + u_j\frac{\partial u_i}{\partial x_j} = B_i - \frac{1}{\rho}\frac{\partial P}{\partial x_i} + \frac{1}{\rho}\frac{\partial \tau_{ji}}{\partial x_j} \tag{3.7}$$

Betz Limit

As used earlier in a previous study [16], the turbine can as well be represented by a plane of disc in order to make a couple of assumptions and most importantly, approximate results are obtained in the replacement of a turbine with a disc actuator for cfd analysis.

Assumptions taken are;
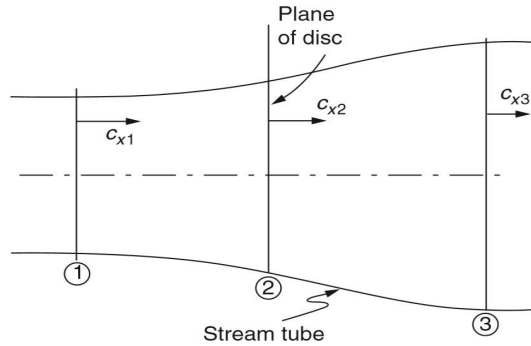
Figure 3.1: Flow over a plane disc [38].

1. Incompressible flow

2. Steady uniform flow upstream of the disc

3. Uniform and steady velocity at the disc

4. No flow rotation produced by the disc

5. Flow passing through the disc from the upstream and downstream is within the stream tube.

Axial velocities of the water current flow;
upstream = c_{x1}
disc = c_{x2}
downstream = c_{x3}
From the continuity equation, the mass of the water current flow is;

$$m = \rho c_{x2} A_2 \qquad (3.8)$$

where;

$$\rho = \text{Density of water}$$
$$A_2 = \text{the area of disc}$$

Axial force acting on disc;

$$X = \dot{m}(c_{x1} - c_{x3}) \qquad (3.9)$$

And the power extracted by the turbine is

$$P = Xc_{x2} = \dot{m}(c_{x1} - c_{x3})c_{x2} \qquad (3.10)$$

Therefore, energy lost by the water current flow will be;

$$P_w = \frac{\dot{m}(c_{x1}^2 - c_{x3}^2)}{2} \tag{3.11}$$

Assuming no other energy loss; Power lost by water current flow, P_w = Power extracted by the turbine, P

$$\frac{\dot{m}(c_{x1}^2 - c_{x3}^2)}{2} = \dot{m}(c_{x1} - c_{x3})c_{x2} \tag{3.12}$$

$$c_{x2} = \frac{(c_{x1} + c_{x3})}{2} \tag{3.13}$$

This is to show that the velocity of the water current flow in the disc plane is the average of the velocities far upstream and far downstream of the disc with wake mixing being ignored. However, the power coefficient, C_p which is a measure of the tidal turbine efficiency and can be measured basically as the ratio of the mechanical power produced to the power available in the water current flow at specific velocity.

Therefore, power coefficient,

$$C_p = \frac{P}{P_0} = 4a(1-a)^2 \tag{3.14}$$

Differentiating C_p with respect to a,

$$\frac{dC_p}{da} = 4a(1-a)(1-3a) = 0 \tag{3.15}$$

Therefore,

$$a = \frac{1}{3} and 1 \tag{3.16}$$

The Bertz limit which is the maximum power that can be extracted from the water current flow notwithstanding the design of the turbine can be calculated using the first value. And the maximum power coefficient which is also referred to Betz limit is;

$$C_{pmax} = \frac{16}{27} = 0.593 \tag{3.17}$$

This theoretically means no turbine can convert more than 59.3 percent of the kinetic energy in a tidal current into into mechanical energy to cause rotation of turbine rotor [39].

3.1.3 Power, Lift and Drag

In the performance analysis of a turbine, there are some important terms to be defined in order to obtain the required results. The Tip-speed ratio which can be defined as the ratio of the speed of the rotating blade tip to the speed of the free stream wind can be represented mathematically as;

$$TSR, \lambda = \frac{\omega R}{V} \tag{3.18}$$

Where ω, which is the angular velocity $= 2\pi n$ and n is the number of rotations per second, λ is the rotational speed in rad/s, V is the flow velocity and R is rotor radius.

The generation of power by the turbine is dependent on the mass of water current flow passing through the rotor area A of a turbine at a given velocity per second. Therefore, the power output of the turbine in watts will be:

$$P_{out,} = \omega T \tag{3.19}$$

where T is torque.

Power coefficient, C_p expresses the fraction of the power in the water current that is converted by the tidal turbine to mechanical work. It is represented mathematically as

$$Power\,Coefficient, C_p = \frac{power\,output\,from\,the\,water\,current\,flow}{power\,available\,in\,the\,water\,current\,flow} \tag{3.20}$$

With a theoretical maximum value of 0.593 as stated in eqn 3.30.

Therefore,

$$PowerCoefficient, C_p = \frac{\omega T}{0.5\rho A_{ref}V^3} \tag{3.21}$$

Where ρ is the fluid density, A_{ref} is the reference area, V is the incoming velocity.

There is an optimal angle of attack which creates the highest lift to drag ratio. It is dependent on wind speed, hence, it is an optimal TSR as well. Solidity is the ratio of total rotor planform area to total swept area. Low solidity (around 0.1) equals high speed and low torque, while high solidity (> 0.8) equals low speed and high torque.

Theory of Torque in relation to Efficiency (Cp)

To effectively describe the dynamics of a rotating rigid body, the torque is an important parameter employed. To put this into perspective, the concept of torque can literally be described as the force exerted from the rotation of an object about an axis as can be seen in Fig 3.2 below and can be measured in Newton-meters. It is also pertinent to know that torque becomes greater when the Distance and Force components are increasing.
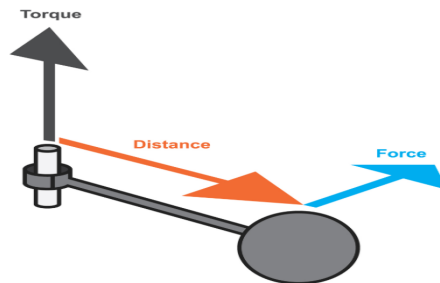
Figure 3.2: Description of Torque [2].

Right hand rule

In order to determine the direction of the angular velocity of a rotating object, the right hand rule comes in handy putting into consideration the direction of rotation.
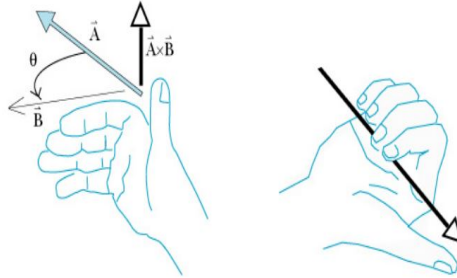
Figure 3.3: Right hand rule [11]

Rotational motion is however not the same as linear motion, but are related in ways that oppose intuition. In Fig 3.3 above, starting with the fingers of the right hand at the axis of rotation, then bending the fingers towards the line in which the force of rotation acts on the object with the thumb sticking out, the thumb indicates the direction of the torque. However, with regards to the direction of the force, the thumb pointing outwards means positive angular acceleration while thumb pointing inward means a negative angular acceleration.

3.1.4   Flow over immersed bodies

According to Çengel and Cimbala, fluid flow over solid bodies frequently occurs in practice, and it is responsible for numerous physical phenomena such as the drag and lift force acting on structures and models [44]. Therefore, this section discusses independent and distinct features that defines the flow around a body (in this case an airfoil) submerged in fluid and the reactions of these features as a result of the disruption caused by presence of these bodies in their path, and also the consequent effect of the external flow on these bodies. However, as a result of the complications of equations guiding flow over bodies, to achieve the aim of obtaining critical knowledge and details, it's inevitable to resort to experimental approach although on a much smaller scale to the actual model (15).

The external flow over airfoils in the figures displayed in the Fig. 3.4, 3.5 and 3.6 shows extreme and undeniable effect and operations of pressure and velocity distribution in order for the airfoil to generate lift (which is force component at right angle to the direction of flow) and drag (which is force component at in line to the direction of flow.
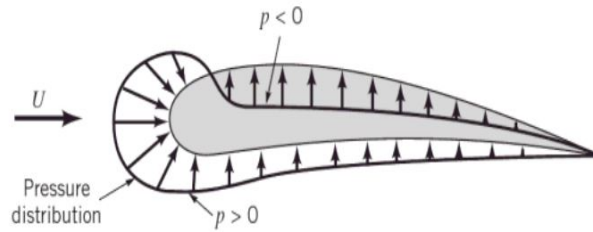
Figure 3.4: Pressure Distribution over the surface of an airfoil [1]
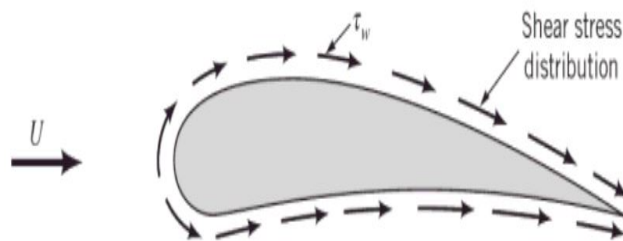
Figure 3.5: Shear stress Distribution over the surface of an airfoil [1]
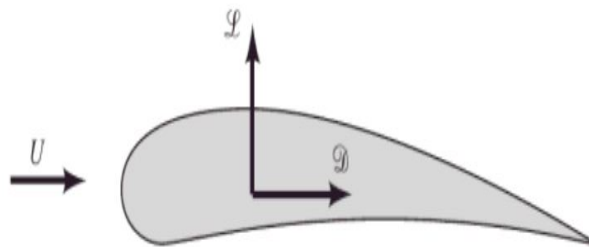
Figure 3.6: Lift force and Drag force direction in relation to incoming flow [1]

3.2 Blade element momentum Theory

One of the oldest theory applied in the calculation of velocities on the blades of wind turbines is the Blade element momentum (BEM) as it is a development on the actuator disc theory of the pioneered 19th century propeller work of Rankine and Froude [27]. In Blade element theory, the propeller blade which is made up of a combination of different airfoils are separated into sections, to which a force balance is applied to individual sections to generate lift and drag. These generated lift and drag are then summed up to obtain thrust and torque for the propeller blade. The application of the blade element theory aims at reducing the challenges associated with the modelling of complicated 3-dimensional flow

with the assumption that a linear summation can be utilized in it's stead, which accounts for the analysis of flow over the divided sections or elements of the blade [42]. The origin of the BEM theory emerged from the blade element theory and the momentum theory even though it was conventionally credited to Betz and Glauert (1935) who was believed to introduce the analytical model by combining the blade element and the momentum theory [9]. Therefore, to utilize the full potential of the tidal current energy, the BEM technique is used in this study and the results obtained was validated using an online software Qblade.

The propeller generated thrust is the propeller reaction in relation to the momentum change the propeller transfers on the flow through it. In other words, the rate of momentum change is the product of mass flow rate and the change of velocity of flow influenced by the propeller. Therefore, the movement of a great mass of flow in relation to a small change in velocity can generate a great thrust [42]. However, with the order reversed, the same great amount of thrust can also be generated by the movement of a small mass of flow in relation to a greater velocity. As a result, the momentum theory is able to predict the efficiency of moving a great mass of flow by only giving to it a small change in velocity [42].

From the equation below, axial force can be generated from the momentum theory with the assumption that power can be generated from the blades without rotary motion

$$dF = 4a(1-a)\rho_a V^2 \pi r dr \qquad (3.22)$$

$$a = \frac{V - V_T}{V} \qquad (3.23)$$

Where a the axial induction factor, ρ_a is air density, V the wind velocity far downstream and r the distance of the element from hub and V_T is the wind velocity far upstream.

With the introduction of the rotational motion to generate thrust, the equation becomes;

$$dT = 4a'(1-a)\rho_a V\Omega\pi r^3 dr \qquad (3.24)$$

$$a' = \frac{\omega}{2\Omega} \qquad (3.25)$$

Where Ω is the angular speed, ω is the rotational speed of the blade and a' is the angular induction factor.

To generate the concluding equation that makes the relation on which the BEM theory presides over the design of the propeller blade, the Blade element theory which estimates the thickness of the blade sections as immeasurably minute and also taking into consideration the aerodynamic independence and non interference between these rotor blade sections, we have the following Blade element theory relation.

$$dF = \frac{1}{2}\rho_a BCW^2 dr[C_L cos\phi + C_D sin\phi] \qquad (3.26)$$

$$dT = \frac{1}{2}\rho_a BCW^2 rdr[C_L sin\phi + C_D cos\phi] \qquad (3.27)$$

where C_L and C_D are the lift and drag coefficients respectively, ϕ is the angle of flow, B is the number of blades, W is the velocity and C is the chord.

Equating equations 3.31 and 3.35, we have;

$$8a(1-a)V^2\pi r = BCW^2[C_L cos\phi + C_D sin\phi] \qquad (3.28)$$

Also, equating equations 3.34 and 3.36, we have;

$$8a'(1 - a)V\Omega\pi r^2 = BCW^2[C_L sin\phi + C_D cos\phi] \tag{3.29}$$

3.3 CFD simulation

The application of Computational Fluid Dynamics (CFD) is the combination of knowledge, skills and impressions acquired from the study of physics, fluid flow, softwares, mechanics and arithmetic, aimed at discretizing governing equations (like Navier stokes Equation or Reynolds-Averaged Navier-Stokes equations in most cases) and solving with suitable numerical schemes, thereby satisfying the laws of conservation of mass, momentum and energy to predict the behavior of the fluid. With great and on going improvement over the years, CFD has present itself as a functional and handy tool for investigating and predicting fluid behavior in a defined space domain. Also, CFD simulation can be employed to analyze and reconstruct the performance of a model with specific boundary conditions [32]. To numerically find solution to a partial differential equation, the proposed geometry of the domain to be analysed is first created, then divided into elements before being subjected to discretization [32]. However, achieving an accurate simulation result is dependent on a number of factors which ranges from refining the mesh which is the divided elements known as mesh resolution, utilizing a lower time step size and reliable time step parameters, and also numerical schemes relatable to Boundary conditions.

3.3.1 Laminar and Turbulent flow

Osborne Reynolds (1842 - 1912) conducted an experiment that brought about the important classification of fluid flow into Laminar and Turbulent [3]. Among different categories fluid flow can be categorized, Laminar flow and Turbulent flow will be discussed as a result of the activities of these phenomena in relation to fluid behaviour at distinct layers of flow.
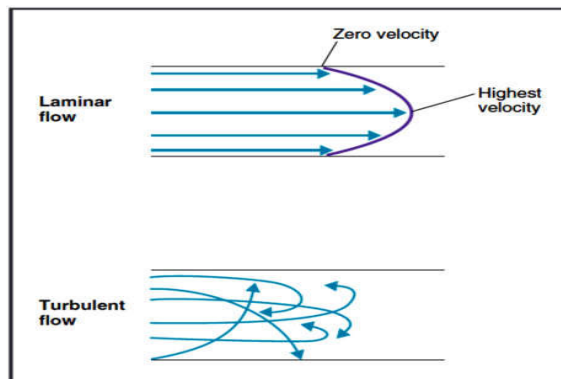
Figure 3.7: Laminar and Turbulent Flow [23]

Laminar flow can be described as a smooth and undisturbed flow of parallel layers of the fluid as shown in Fig 3.9 and it occurs at low fluid velocities. It is caused mainly by the presence of strong viscous forces at these low velocities in layers of fluid flow. As a result of these forces, a resistance is experienced in the flow of layers close to each other with the greatest resistance taking place at the wall of the geometry where fluid layer is stationary and where exchange of mass and momentum is also experienced [20]. As can be seen from Fig 3.10 below the boundary layer thickness on the y-axis and the flow rate on the x-axis also shows laminar flow behaviour. Skin friction which is an exerted resistant force as a result of fluid viscosity for laminar flow is given by;

$$C = \frac{0.664}{\sqrt{Re_x}} \tag{3.30}$$

where Re_x is the Reynolds number
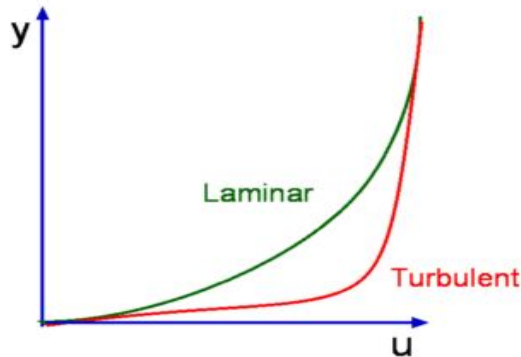
Figure 3.8: Velocity profile of Laminar and Turbulent flow [3]

Turbulent flow on the other hand as shown in Fig 3.9, is a category of flow exhibiting small fluid elements with circular or half circular movement known as eddies rapid and disturbed motion in several layers. As a result, the pressure drops and energy dissipation is experienced by reason of increased velocity [20]. The velocity profile displayed in Fig 3.10 with the boundary layer thickness on the y-axis and the flow rate on the x-axis also shows turbulent flow behaviour.

Skin friction which is an exerted resistant force as a result of fluid viscosity for turbulent flow given by;

$$C = \frac{0.0594}{\sqrt{Re_x}} \tag{3.31}$$

where Re_x is the Reynolds number
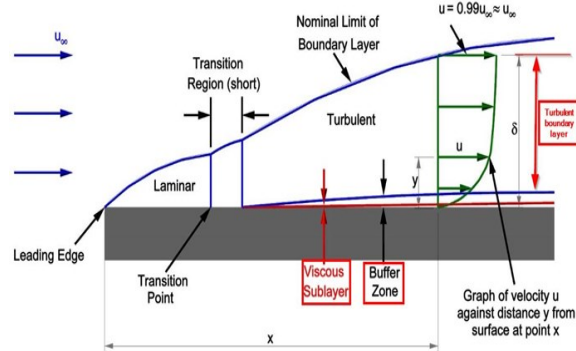
Figure 3.9: Development of Laminar and Turbulent Flow at Boundary layer [5]

3.3.2 Reynolds number

Reynolds number is applicable to resolve numerous challenges related to fluid dynamics or flow. It can be used to distinguish between laminar and turbulent flow which are two different flow patterns. In laminar flow where Reynolds number less than 2300, the velocity field evolves steadily and the streamlines move in parallel. Whereas, in turbulent flow with Reynolds number greater than 4000, significant unsteadiness in the velocity and pressure field is experienced. It is also applicable in the validation of Bernoulli principle. From the mathematical relation;

$$Re = \frac{v \cdot d}{\nu} = \frac{inertial\,force}{viscous\,force} \tag{3.32}$$

From Eqn 3.32, if the Reynolds number is huge, this simply means the momentum force is big relative to the viscous forces on the foil and vice versa. Also, Reynolds number helps to correlate the values of the lift and drag forces acting on the airfoil.

3.3.3 OpenFoam

Fluid flow, heat transfer and chemical reactions systems can be analysed with the use of computer based simulation software like OpenFoam which is an open source software written in c++ code and it's software can be accessed and modified by the user

The main objective motivating the advancements experienced in the CFD field is to build a capability that is comparable to other CAE (computer-aided engineering) tools such as stress analysis codes.Although still in it's developing phase, it presently cannot be used ignorantly and the reason CFD has lagged behind is the tremendous complexity of the underlying behavior of fluid flows [8]. Below is an overview of the openFoam structure and process.
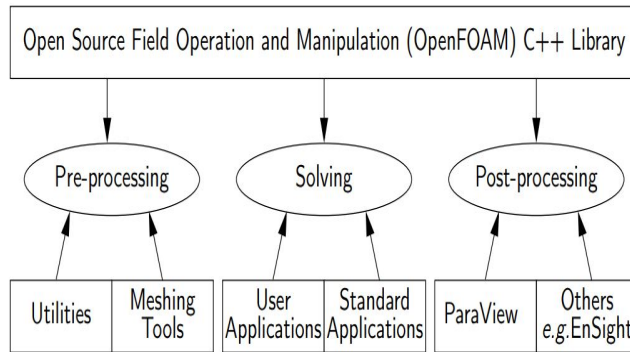
Figure 3.10: openFoam structure [17]

3.3.4 blockMesh

blockMesh is a multi-block mesh generation utility located in the blockMeshDict dictionary, in the system file of an openFoam case. It makes use of the instruction in this dictionary to generate and outputs the mesh data in points and faces, cells and boundary files in the same directory [17].
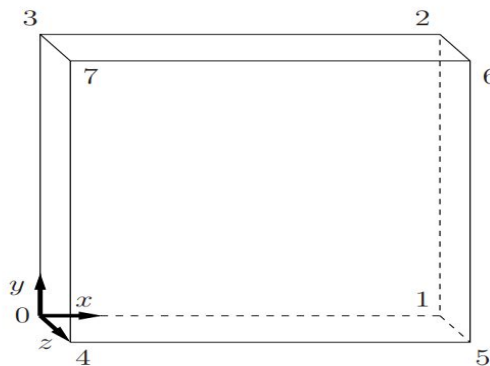
Figure 3.11: blockMesh coordinate system [17]

3.3.5 SnappyHexMesh

SnappyHexMesh is a meshing tool available in openFoam that makes use of stl files and waveobject (obj) files in which the geometry and domain must be defined. Before the execution of snappyHexMesh, a background mesh carried out by blockMesh and which is made up of Hex cells fill the whole domain is created. With the figures beolw, the process of meshing with snappyHexMesh as a meshing tool will be further explained.

During the process of mesh generation using snappyHexMesh, Fig 3.12(a) displays
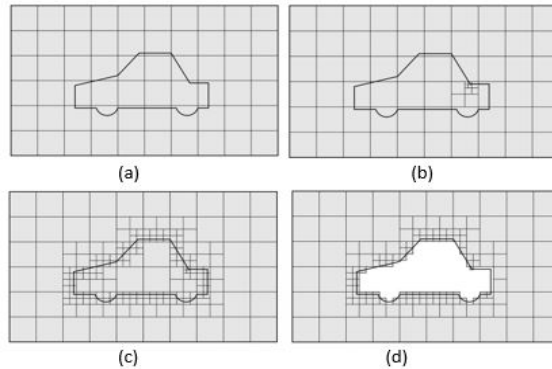
Figure 3.12: snappyHexmesh process of meshing [17]

the initial mesh generation also known as the background mesh, where the mesh is made up of hexes. Splitting of the cells in respect to the specified edge features in the domain commence in Fig 3.12(b). Afterwards, the process of cell removal as displayed in Fig 3.12(c) starts. However, it should be noted that this process requires a confined and encased surface within the domain and the cells with more than half of their volume lying in the enclosed geometry are retained. A confined surface is important as the next operation carried out by snappyHexMesh is the removal cells which entails discarding of the cells present inside the confined model, thereby, further splitting the cells within the enclosed geometry as shown in Fig 3.12(d) [17].

Other operations carried out by the sub dictionary are castellatedMeshControl which is made up of files and refinement level for the featureEdgeMesh and the refinement Surface by splitting cells in relation to the designated or defined edges of the geometry/model inside the domain and the established refinement level stated in the castellatedMeshControls is responsible for how refined the model surface is [17].

3.3.6   Boundary Condition

Boundary conditions are the initial data fields located in the 0 folder which is set up after mesh generation. There are three essential entries in the initial field files. These entries are;

1. dimensions: The dimensions of the field are defined in this entry.

2. internalField: this can either be set to uniform or nonuniform,

3. boundaryField: this includes the boundary conditions including information for all the boundary patches.

In this research work, information on the Boundary conditions used can be found in the Appendix section.

3.3.7 Time step

The influence of time step in the accuracy of CFD simulation results and also in the enhancement of its convergence cannot be over emphasized. In order to accurately simulate the dynamic rotational motion of a turbine, there are various settings of time step that can be utilized [13]. Primarily, the time step is appointed as measure to capture the physical developments involved in the simulation. The figure below shows how at one degree per time step, rotation of a turbine as it achieves a full rotation of 360 degrees around the swept area.
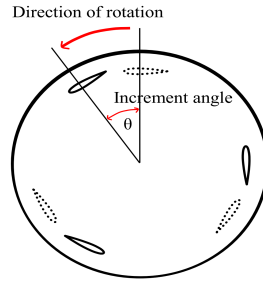
Figure 3.13: Time step representing increment angle for each rotational degree [13]

3.3.8 Courant number

In the solution of partial differential equations, Courant number which is a non dimensionless number is very important. As a result of the implicit discretization in OpenFOAM, the Co no longer serves as a measure of stability, rather, it is more in line with the accuracy of the simulation as Co is best kept at less than or equal to 1. To show its reduced strictness towards stability, Co greater than one results in a very high time step which literally means that the particles of the fluid moves across more cells at this large time step. By reason of not strictly moving through the cells, the accuracy is greatly reduced, however, the solution is still considered as stable [40]. It can be mathematically represented by;

$$C = \frac{U\Delta T}{\Delta x} \tag{3.33}$$

Where C is the courant number, Δt is the time interval, U is the dependent variable and Δx is the distance between two consecutive nodes.

3.3.9 AMI

A stationary mesh is mostly utilized in majority simulation cases in CFD. However, AMI which is a totally new technique is employed in order to be able to numerically analyze rotating mesh

At the boundary condition type of cyclicAMI, the Transform which describes the operation to map the neighbour patch to the owner patch options are:

1. noOrdering: This literally means that the operation is determined by the patch and no mapping is defined.

2. coincidentFullMatch: no transform defined and this check that the patch faces are matched.

3. rotational: this rotates about an axis of rotation.

4. translational: the movement here is translational.

Figure 3.14: AMI technique using cylinder to effect rotary motion

3.3.10   y+ value

Yplus value can be literally described as the size of the cell closest to the boundary of the model to be simulated in relation to the fluid flow. This number helps you to know where is your first cell center compared to the boundary layer thickness.
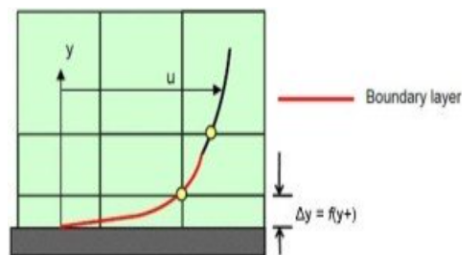
Figure 3.15: y+ Description [7]

From fig 3.8 above, a boundary layer is composed of different sections and the section closest to the wall is dominated by viscous effects which is the viscous layer. In order to generate an accurate simulation, the first cell center must be inside the viscous layer. However, it is usually considered that a y+ smaller than 4 is required, but y+ smaller than 1 is ideal.

It is however also important to note that the first cell size matches the chosen turbulence model.Turbulence model RAS k-omega SST needs a yplus that is smaller than 1 while turbulence model k-epsilon needs a y+ between 30 and 60. The mathematical description of y+ is defined below;

$$y^+ = \frac{u_* y}{V} \tag{3.34}$$

where y+ is the non-dimensionalized distance from the wall, u* is the friction velocity, y is the vertical distance to the nearest wall and V is the fluid's kinematic velocity.

In order to generate the y+ value, the velocity has to be firstly computed, thereby making it a postProcess procedure.

3.4   Turbulence Model

The fundamental factors in CFD after generation of grid and algorithm is turbulence modeling which according to Taylor and von Karman's proposed definition of turbulence in 1973, *"is an irregular motion which in general makes its appearance in fluids, gaseous or liquid, when they flow past solid surfaces or even when neighboring streams of the same fluid flow past or over one another"* [10]. The concept of Reynolds averaging and the averaged conservation equations are some of the main concepts that form the basis of turbulence modeling. Turbulence occurs at high Reynolds number since all turbulent flows are three-dimensional, irregular, transient and unstable flow. A set of equations can however be used to represent a turbulence model in order to determine the turbulent transport terms in the mean flow equations [10].

In turbulence modelling, we have the one-equation model and two equation model. The two-equation models which are commonly used are either the k- ω model or the k-ϵ model. These two models evaluate the transport equations in order to determine eddy viscosity as an expression of turbulent kinetic energy and it's dissipation rate [36]. Both the models however rely on an assumption that eddy viscosity can be related to a time and length scale that describes turbulence. Also, it is worth noting that the major difference between these two models is in the trend of ω and ϵ at the wall and their definition of the wall boundary conditions [36].

3.5   Other softwares used

In the actualization of the aim and objectives of this research work, a couple of other softwares were utilized to achieve desired model design to be used for simulation.

3.5.1   Inventor

This is a 2D and 3D Mechanical Engineering CAD software that can be employed to design, visualize and simulate models.

3.5.2 Qblade

The software Q-Blade is a human friendly and flexible open source rotor blade design and calculation software that enables the design and computation of an airfoil's polar performance and directly integrates with the turbine rotor design and simulation [41]. QBlade is developed as an open source software mainly utilized for the simulation and design of horizontal and vertical axis wind turbines efficiency making use of BEM [25]. Fig. 3.10
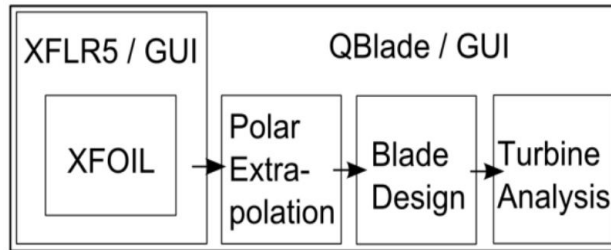
Figure 3.16: Qblade software modules [25]

displays the modules that makes up the Qblade software which plays different roles in the design of custom airfoils and the computation of airfoil lift- and drag coefficient polars the viscous-inviscid coupled panel method code XFOIL is integrated within the graphical user interface of QBlade. Additionally, a module for the extrapolation of airfoil polars, beyond the stall point and for a 360 degrees range of angle of attack is integrated. The resulting functionality allows the use of QBlade as a comprehensive tool. Also, the constant maintenance, validation and advancement in functionality makes it a viable tool.

Q-Blade also gives deep insights into all the relevant rotor and blade variables with its post processing functionality. Software is very flexible and has user friendly interface for wind turbine rotor blade design.

In Q-Blade Three rotor blades have same design and 3D rotor can be created from the single blade design. Further, power simulation is carried out on the rotor blades. Rotor BEM simulation is used with simulation parameters tip speed and Reynolds number. A rotor simulation can only be defined when any rotor blade is present in the runtime database. When defining a rotor simulation, the the DMS algorithm and the simulation parameters has to be selected to the desired corrections. Once a simulation is defined, the user can select a range of tip speed ratios and the incremental step for the simulation. Analysis is performed based on the obtained simulation graphs and blade design is varied for further modelling.

3.5.3 Pointwise

Although, Pointwise is another meshing tool made use of in this research work, it's process is very different from that of snappyHexMesh as it makes use of Graphics User Interface for it's mesh construction. Depending on dimension of the geometry or model to be meshed, Pointwise accepts CAD models in stl format for 2D geometry and stp or obj

format for 3D as the maximum number of facets in stl Pointwise can work on is 10,000 which makes 2D stl geometries suitable to be meshed while most 3D mesh construction can be carried out on other CAD format.

3.5.4   postProcess tool: paraview

ParaView is an open-source application for visualizing two- and three- dimensional data sets which can handle varies widely depending on the architecture on which the application is run. Basically, it is a tool used to analyze results and visualize them in order to further have a comprehensive understanding of what is happening in the predefined domain [21].

Using the terminal in OpenFOAM, Paraview can be launched with the script "paraFoam" and can be executed like any of the OpenFOAM utilities [17]. Also, generated results viewed in Paraview can be influenced to be displayed at desired resolution and pattern.

Chapter 4

Methodology: Framo Base Propeller case

As mentioned earlier, the decision to design an open stream domain designed for this research analysis as shown in Fig 4.1 was borne out of the desire to imitate a scenario as close as possible to what the tidal turbine would experience while in operation as well as observe the reaction of the flow over the open center propeller designed by Framo AS.

4.1 Experimental set up

As a result of the COVID-19 situation, the scheduled participation in small-scale testing at Framo AS laboratory was not possible. However, the geometry model received from Framo AS which is a free standing CAD designed propeller of 0.168m diameter is the same model used for the CFD analysis.

4.2 CFD Case Setup

4.2.1 Free stream

Mesh generation

A good mesh is the foundation to obtain an accurate output when it comes to CFD simulations. Bad quality in mesh results in divergence of the solver which either crashes or

Table 4.1: Design specification of Framo AS propeller

Duct Specification	Specification
Propeller Diameter	0.168m
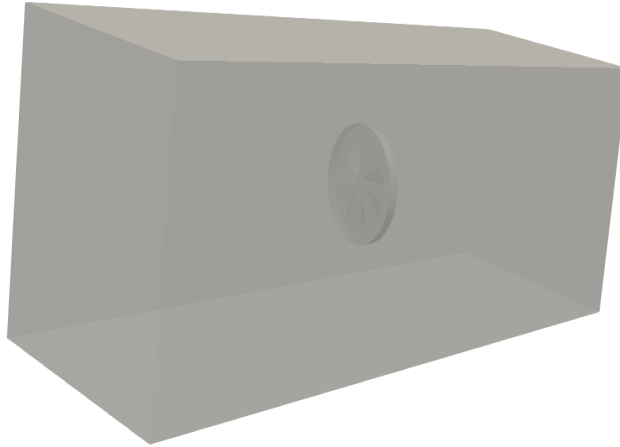
Figure 4.1: Computational domain.

Table 4.2: Open center propeller mesh sensitivity study.

Grid	Number of cells
Coarse	4,417
Mild	9,401
Fine	174,372
Very fine	405,912

leads to incomplete solution of the task. A similar case was experienced in this research work as attaining a good mesh quality became a challenge and time demanding with the snappyHexMesh meshing tool employed for the generation of mesh in this setup.

Mesh study for the computational setup of the Framo AS open center propeller

In order to find a reasonable grid size for the simulation, a grid study using four different mesh conditions with the set parameters designed for the turbine which are 2.54m/s for velocity and 62.83rad/s for the angular velocity (ω).

The mesh generated as can be seen in Fig 4.2 at different number of cells showing how accurate each number of cells can effectively generate mesh around the geometry taking into account all surfaces, edges and corners. The fine mesh will be chosen for the simulation analysis as number of cells greater than this will lead to a longer computational time with the same result as the fine mesh chosen.

In Fig. 4.2, coarse mesh on the top right over the curved geometry and the blade can be seen to be inadequate and sparsely distributed at a very low number of 4,417 cells.

Also, the mild level mesh is not adequate enough for the tip and edges around the blade resulting in spikes around the blade at a low number of 9,401 cells.
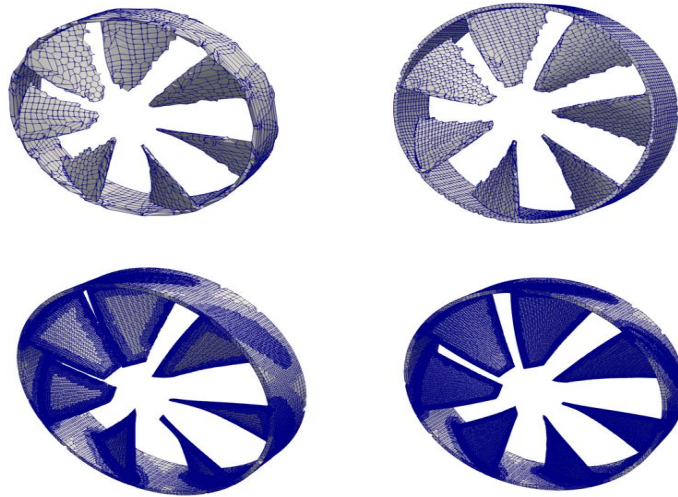
Figure 4.2: Analysis of mesh study (Top right: Coarse, Top left: Mild, Lower left: Fine, Lower right: Very fine)

However, the fine mesh accounts more for the edges and curved geometry around the blade as the number of cell increases to 174,372 cells accounting for all curved and sharp edges around the geometry.

A higher number of 405,912 cells also created a finer and uniformly distributed mesh on the blade surface

4.3 Bi-Directional Duct Design consideration

As mentioned in chapter 2, the duct design for analysis in this research was obtained from a previous research work carried out by Giljarhus [16].

From the schematic diagram in Fig 4.3, the length of the duct is 2 times bigger than the propeller diameter and the duct inflow diameter is 1.5 times bigger than the propeller diameter, with a duct thickness of 0.01m.

Afterwards, inventor was employed to develop the 3D CAD model as seen on the right in Fig 4.3
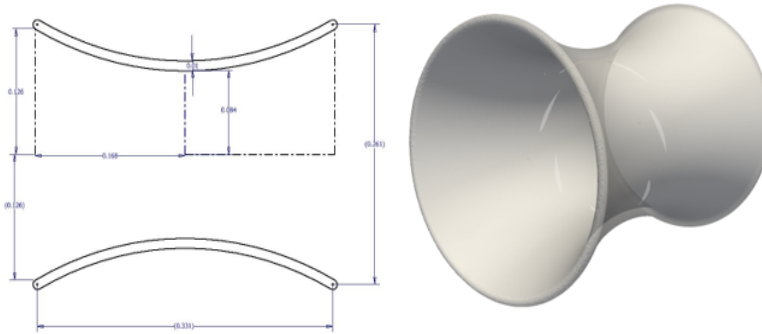
Figure 4.3: Duct cross section (on the right in (m)) and CAD model of Duct

Table 4.3: Open center Duct propeller mesh sensitivity study.

Grid	Number of cells
Coarse	19,578
Mild	138,723
Fine	299,964
Very fine	474,258

4.3.1   Mesh study for the computational setup of the open center propeller Bi-directional Duct

As displayed in Fig 4.4 above, a grid analysis was also carried out on the ducted turbine in order to examine how accurate the number of cells were able to mesh the geometry. The mesh over the propeller and duct at a very low number of 19,578 cells generated a coarse level of mesh, while n increase in cell number to 138,723 on the surface of the duct and propeller, edges and curves on the propeller blades are being taken cared of but cells at the curved edges of the duct are still not uniform.

Increasing the cell generated number to 299,964, all edges are accounted for creating a uniform distribution of cells on the geometry.

The very fine grid level increased number of cells to 474,258 resulting in a more refined cell distribution.
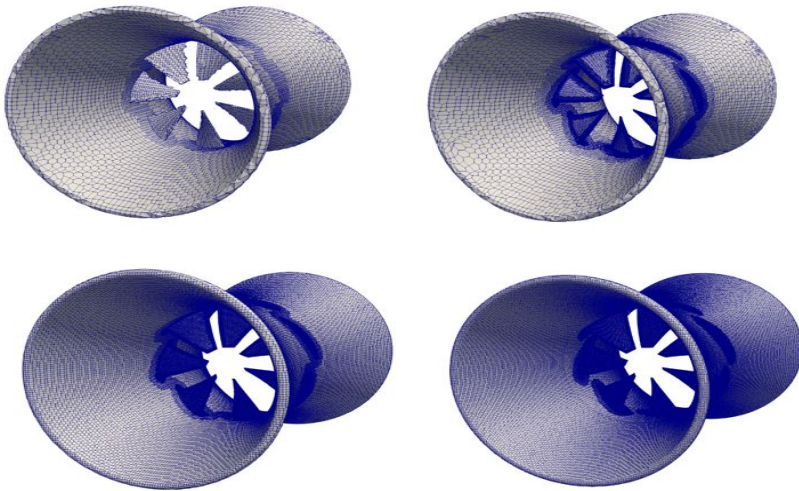
Figure 4.4: Analysis of mesh study (Top right: Coarse, Top left: Mild, Lower left: Fine, Lower right: Very fine)

5

Methodology: MHKF Turbine

5.1 Marine Hydro Kinetic Foil Blade

The turbine to which the MHKF hydrofoil are utilized, are designed uniquely for horizontal axis turbines in order to enhance the performance of these turbines. Compared to wind turbine where this technology originated, the high density of the fluid loading on the tidal turbine in relation to that of wind turbine is much higher, making the hydrodynamic forces acting on the tidal turbines greater than the aerodynamic forces on wind turbines. Therefore the blade sections of hydrokinetic turbines should be relatively thicker than that of wind turbines. Figure 5.1 below displays the cross sections of the MHKF1 blade, exhibiting the foil profiles complexities. [4] .
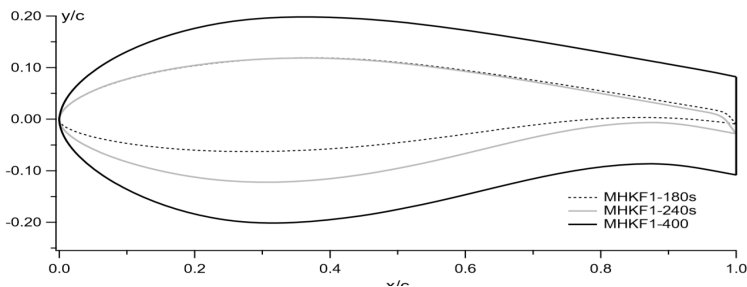
Figure 5.1: Family of MHKF1 Hydrofoil [6]

However, there are numerous MHKF1 foil profiles in the hydrofoil family and the MHKF1-400, MHKF 240s and MHKF 180s were used specifically based on the requirement of the validation experimental research studied to verify this research work. Moreover, two objectives were apparent in the sandia research used for validation in this project work. First, to attain high lift and minimize drag. Secondly, the foils were designed to curtail potential performance complications from soiling or biofouling thereby reducing the possibility of cavitation [6]. Which resonates with the aim of maximizing the

performance of the turbine as well in this research work. In addition, the tip and the mid span of the blade which are the MHKF1-180s AND MHKF1-240s profiles were designed to minimize singing, as a result of the slanting edge rather than sharp edge which due to low frequency noise eliminate resonant vibration bringing about the "s" attached to their names. Also, these anti-singing foil geometries are designed to be asymmetric purpose-fully to introduce separation and vortex shedding towards the trailing edge on the upper chamber while retaining a smooth flow on the pressure side (lower chamber) [6].

5.2 Experimental set up

Propeller design is all about trade offs. The designer tries to create the most efficient pro-peller possible. The principal challenge to this is the direction of water velocity. However, to go from ideal to practical propellers, we need to understand the choices and trade offs of propeller blade design which are complex, with many choices along the way.

The foils were designed to minimize performance losses from soiling/bio- foul-ing and reduce the likelihood of cavitation. In addition, the outboard and mid-span hydro-foils incorporated trailing edge geometries that were designed to minimize singing, a cou-pled hydroacoustic-hydroelastic phenomenon in which thin, sharp trailing edges produce significant high-frequency noise due to a resonant vibration [6].

5.3 CFD Case Setup

Prior to the OpenFoam case setup, the three hydrofoils used in the generation of the long span blade for the turbine was carried out using Qblade. Figure 5.2 shows the arrangement of the MHKF1-180,240s and 400 in blade root to blade tip order.
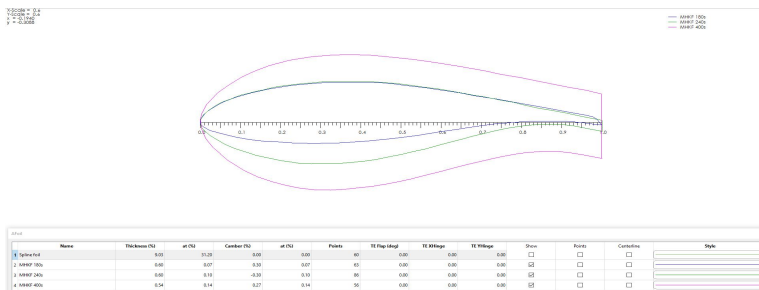
Figure 5.2: Hydrofoil design in Qblade.

5.4 Mesh generation on Hydrofoil profiles: MHKF1-180s, 240s and 400

In order to mesh the hydrofoil profiles, Pointwise was employed as a meshing tool to generate a better quality mesh around the surface of the foils.

Table 5.1: yPlus range for MHKF1-180s, 240s and 400

MHKF Hydroil	yPlus value
180s	5 <y+< 30
240s	30 <y+< 100
400	30 <y+< 100

The y+ value of the mesh around the MHKF1-180s foil was 6.2 which falls in the range of 5 <y+< 30 with an input wall spacing of $5.38x10^-6$, chord length of 1m, density of $1000kg/m^3$ and Reynolds number of $1.5x10^6$. The $y+$ value of the mesh around the MHKF1-240s and 400 foil was 48.6 and 52.93 respectively which falls in the range of 30 <y+< 100 with an input wall spacing of $5x10^-4$, chord length of 1m, density of $1000kg/m^3$ and Reynolds number of $3.33x10^5$.
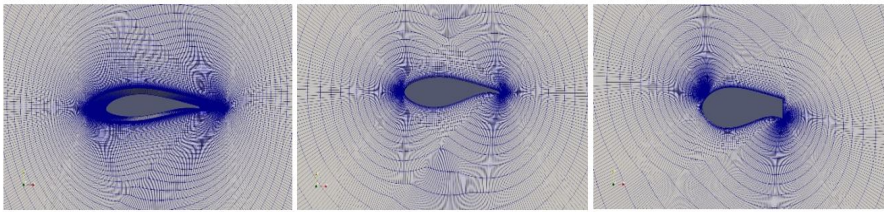
Figure 5.3: (a)MHKF1-180s mesh (b)MHKF1-240s mesh (c)MHKF1-400 mesh

5.4.1 Blade Geometry

The spanwise distribution of the foils from root to the tip (in the order of MHKF1-400, 240s and 180s) as shown in the figure below, the geometry, twist and length of the blade was obtained with a ratio of 1:8.7 which gives the blade a long span length of 0.281m in conformity to the validation case [6] used for this study.
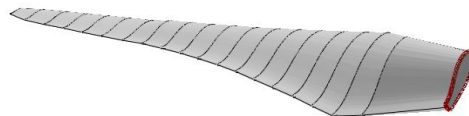
Figure 5.4: Hydrofoil design in Qblade.

Table 5.2: MHKF Turbine specification.

Turbine Specification	Specification
Turbine diameter (D)	0.562m
Hub diameter	0.16
Optimum blade pitch	4°

Table 5.3: MHKF Turbine mesh sensitivity study.

Grid	Number of cells
Coarse	3,960
Mild	6,409
Very fine	925,576

5.5   MHKF Turbine

The long span blade model was later assembled together with the hub design in Inventor and developed into a full 3 bladed horizontal turbine as shown in the figure below, ready for simulation analysis.
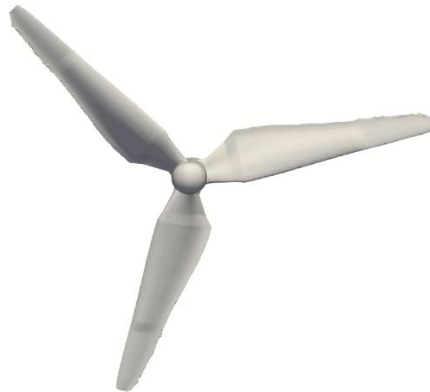
Figure 5.5: MHKF Turbine.

5.6   Mesh generation study for the computational case setup for the MHKF Turbine

In order to find a reasonable grid size, grid convergence study was carried out. Three different cases were analyzed in order to pick a grid size to be used.

Figure 5.6: Analysis of grid study (From left: Coarse,Mild and Very fine).

Table 5.4: Duct specification for MHKF turbine Duct

Duct Specification	Specification
Propeller Diameter	0.562m
Duct Diameter (inlet and outlet)	1.5 * Propeller Diameter
Duct length	2*Propeller Diameter
Duct thickness	0.02m

5.7 Bi-Directional Duct Design consideration

From the schematic diagram in Fig 5.7, the length of the duct is 2 times bigger than the propeller diameter and the inflow diameter is 1.5 times bigger than the propeller diameter, with a duct thickness of 0.02m.

Afterwards, inventor was employed to develop the 3D CAD model as seen on the right in Fig 5.7
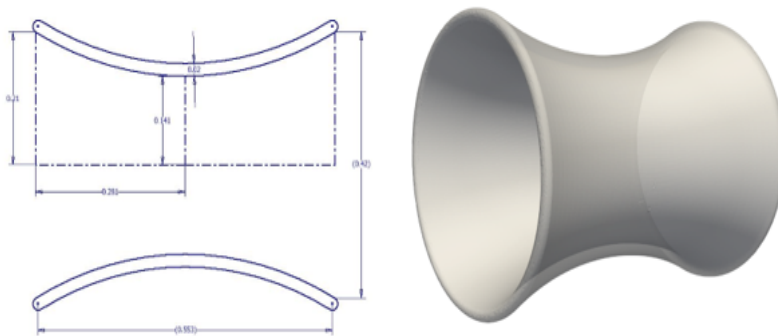
Figure 5.7: Duct cross section (on the right in (m)) and CAD model of Duct.

6

Results and Discussion

This chapter is in two part the project research covered and the results obtained will be discussed.

6.1 Framo Base case

6.1.1 postProcess

Although the mesh is not perfect but gives some reasonable results that can be discussed. The color shows the pressure. Comparing the power coefficient trend and the plots of the flow at 2.54m/s over the blades at three different tip-speed ratios (20.94, 38.22 and 62.83 rads/s), there are two velocity plots, one near the root and one near the tip.
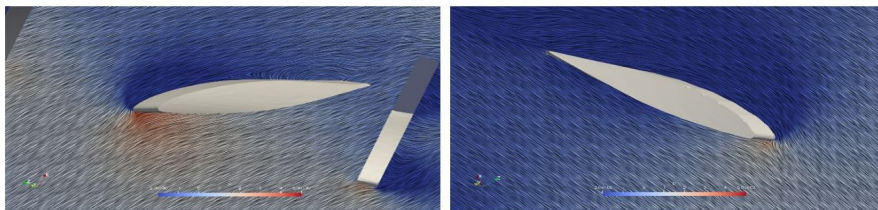
Figure 6.1: at 20.94rads/s, near the blade root (left picture) and near the blade tip (right picture).

At the low TSR, the flow at the root of the turbine blade separates at the trailing edge, which means that the angle of attack is too high.
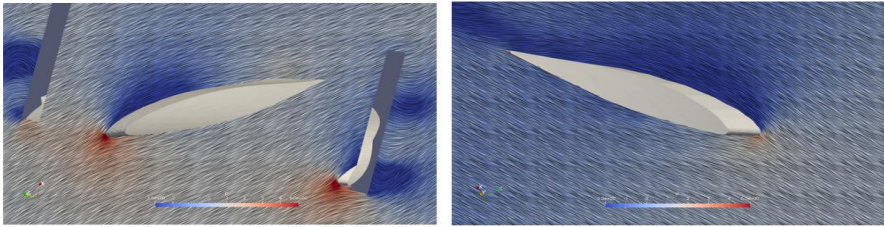
Figure 6.2: at 38.22rads/s, near the blade root (left picture) and near the blade tip (right picture)

At the medium TSR, the flow looks good near the root. It is also better near the tip, but would have higher lift at a slightly higher angle of attack (It is also observed that the pressure difference is not that high between the upper surface and lower surface of the blade).
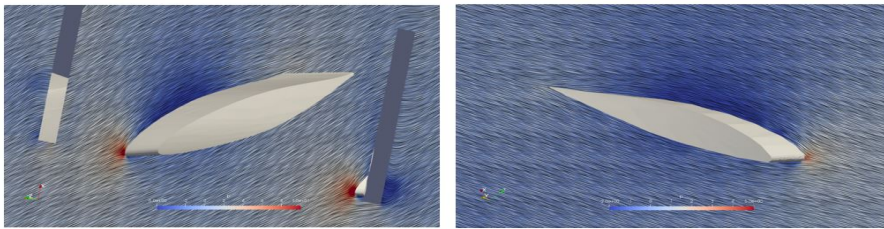
Figure 6.3: at 62.83rads/s, near the blade root (left picture) and near the blade tip (right picture)

At the high TSR, the flow hits at too low of an angle, giving low performance. Also, the pressure is almost the same over and under the blade.

From the plotted power and thrust coefficient against TSR result in Fig 6.4, the highest efficiency was 0.28 which is low. However, a couple of factors ranging from a high angle of attack at a low TSR to the quality of mesh can be attributed to be responsible for this low efficiency generated.
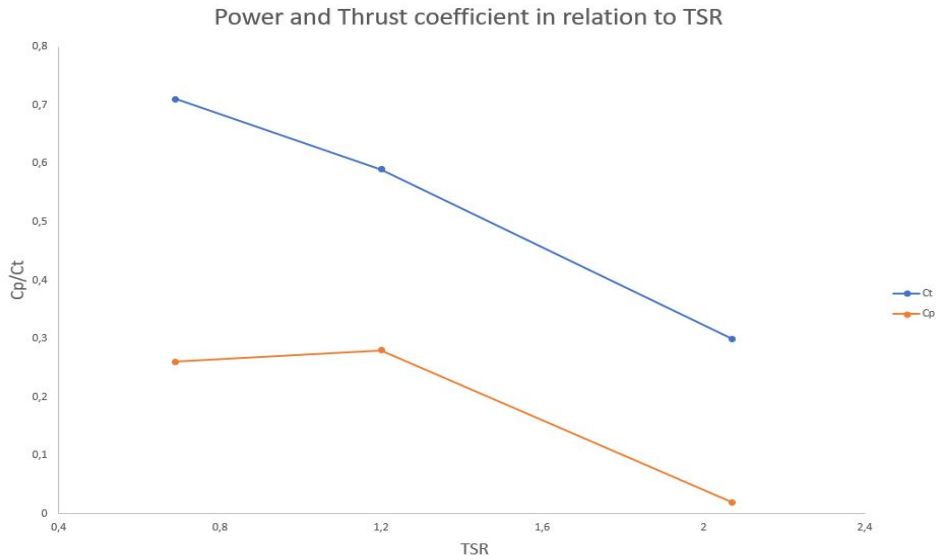
Figure 6.4: MHKF1-180 at -4 degree flow Angle

6.2   MHKF1 Turbine

To determine aerodynamic forces over the foil at specified Reynolds number using the openFoam simulation tool, analysis output for the pressure and velocity distribution by examining the science behind airfoils at varying flow angle over each of the Hydrofoils that makes up the MHKF1 turbine blade will be discussed in this section. It should also be noted that only the incoming flow angle changes as the hydrofoil remain in the same orientation.

6.2.1   CFD simulation analysis of MHKF1-180s at varying angle of attack
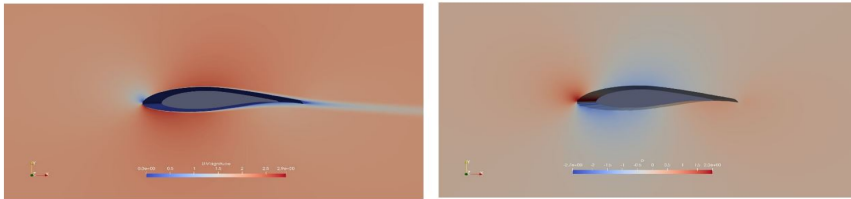
Figure 6.5: MHKF1-180 at -4 degree flow Angle (with velocity plot on the left and pressure plot on the right)

In Fig 6.5, the 180s hydrofoil displays the pressure and velocity distribution of flow at an angle of -4 degrees. It is observed that as a result of the large curvature on the upper surface of the foil, the pressure distribution decreases with an increasing velocity distribution even though a high pressure but low velocity is generated at the leading edge. However, an increase in pressure distribution towards the trailing edge on the lower side of the foil is observed with a corresponding decrease in velocity distribution. And according to Newton's second law of motion, pressure difference across a surface means there is difference in force and this brings about acceleration when no other force stabilizes it as can be seen in the lower surface of the foil. Since lift is generated as a result of the difference in pressure distribution over the upper and lower surfaces, no lift generated at -4 degree angle of attack.
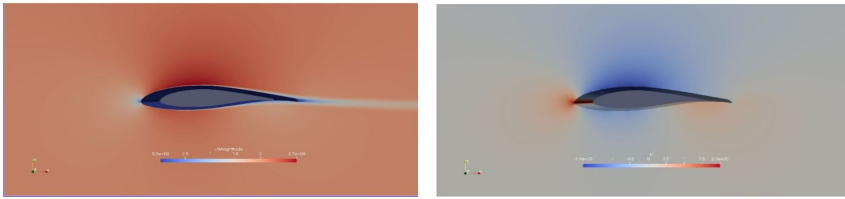
Figure 6.6: MHKF1-180 at 0 degree flow Angle (with velocity plot on the left and pressure plot on the right)

Flow angle of 0 degree over a MHKF1-180s foil also shows a decreasing pressure distribution with an increasing velocity distribution as a result of the high curvature over the upper surface, this brings about deceleration in pressure distribution and acceleration of the velocity distribution. At the lower surface of the foil with lower curvature, the pressure however accelerates towards the trailing edge as there is no other force to stabilize the distribution with a deceleration in the velocity distribution. Since lift is generated as a result of the difference in pressure distribution over the upper and lower surfaces, the lift generated at 0 degree angle of attack is still low.

Figure 6.7: MHKF1-180 at 4 degree flow Angle (with velocity plot on the left and pressure plot on the right)

At a flow angle of 4 degrees in Fig 6.7, the velocity distribution is still high while the pressure flow over the upper surface is low. However, the pressure distribution on the lower surface of the foil can be observed to have an early increase in distribution starting from the leading edge. velocity flow is still converging nicely at the trailing edge of the foil. Since lift is generated as a result of the difference in pressure distribution over the upper and lower surfaces, lift is been generated at 4 degree angle of attack.
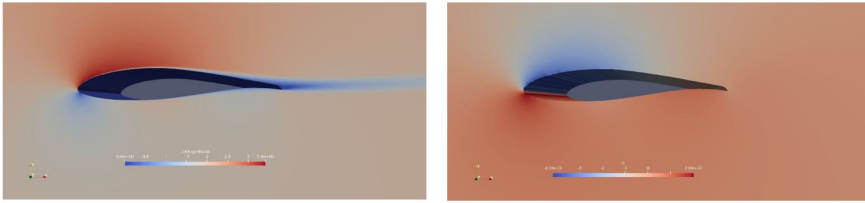
Figure 6.8: MHKF1-180 at 8 degree flow Angle (with velocity plot on the left and pressure plot on the right)

As the angle of attack is getting higher, it can be observed that the pressure distribution decreases to the mid part of the upper surface and starts increasing. However, deceleration can be noticed in the velocity distribution starting also at the mid part of the upper surface towards the trailing edge. Velocity distribution at the lower part of the foil displayed an increase at the mid part but started decreasing towards the trailing edge. This is probably due to the increasing angle of attack. Since lift is generated as a result of the difference in pressure distribution over the upper and lower surfaces, more lift is generated at 8 degree angle of attack.

Figure 6.9: MHKF1-180 at 12 degree flow Angle (with velocity plot on the left and pressure plot on the right)

At flow angle of 12 degrees which is a higher angle of attack, the pressure distribution over the upper surface starts increasing at the leading edge towards the trailing edge while the early deceleration of the velocity distribution can probably be attributed to the high angle of attack whose impact falls on the lower surface of the foil at the leading edge. Since lift is generated as a result of the difference in pressure distribution over the upper and lower surfaces, there is increase in lift generated at 12 degree angle of attack.

Figure 6.10: MHKF1-180 at 16 degree flow Angle (with velocity plot on the left and pressure plot on the right)

Fig 6.10 shows the reaction of the flow with the foil at a flow angle of 16 degrees. It can be observed here also that the velocity distribution over the upper surface of the foil also starts decreasing from the leading edge and at mid part of the foil, wake is generated as the pressure flow accelerates over the upper surface of the foil from the leading edge to the trailing edge. This can perhaps be as a result of the stagnation point moving towards the lower surface of the foil as a result of the a low angle of attack. Since lift is generated as a result of the difference in pressure distribution over the upper and lower surfaces, a decrease in lift generated is experienced at 16 degree angle of attack as the pressure distribution over the surface of the foil is increasing.
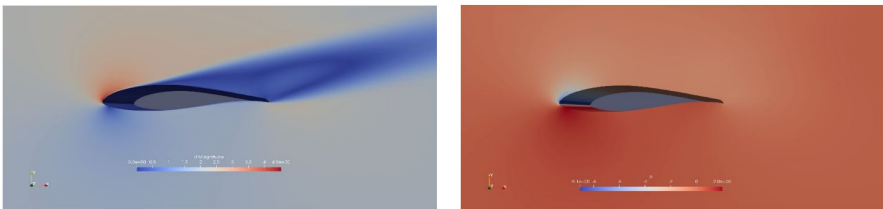
Figure 6.11: MHKF1-180 at 20 degree flow Angle (with velocity plot on the left and pressure plot on the right)

At a flow angle of 20 degrees which is an extreme angle of attack and stagnation point can be observed to be at the lower foil surface, an early separation point can be seen on the velocity distribution over the upper surface creating a large wake greater than previous lower angles of attack. However, with a slight increase in the velocity distribution on the lower surface of the foil, it can be seen that there is a higher increase in the pressure distribution on the foil lower surface. Since lift is generated as a result of the difference in pressure distribution over the upper and lower surfaces, a decrease in lift generated is experienced at 20 degree angle of attack as the pressure distribution over the surface of the foil is also increasing.
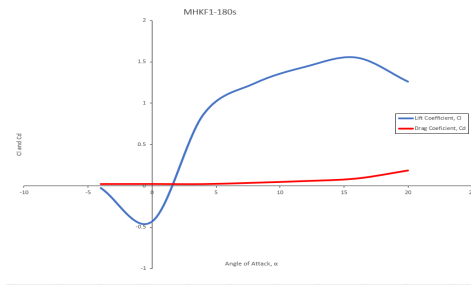
Figure 6.12: Lift and Drag Coefficient against Angle of Attack

After simulations analysis of the hydrofoil MHKF1-180s at varying angles of attack, lift in relation to drag generated at each angle of attack are represented in the plot in Fig 6.12. The plot generated from the Drag and Lift coefficient in relation to the varying angle of attack shows 15.5 degrees as the optimal angle of attack, verifying the results in the pressure and velocity distribution. It can also be observed that the drag coefficient starts increasing at angles greater than 15.5 degrees. It is pertinent to document that this is the foil at the tip of the turbine blade.

6.2.2 CFD simulation analysis of MHKF1-240s at varying angle of attack
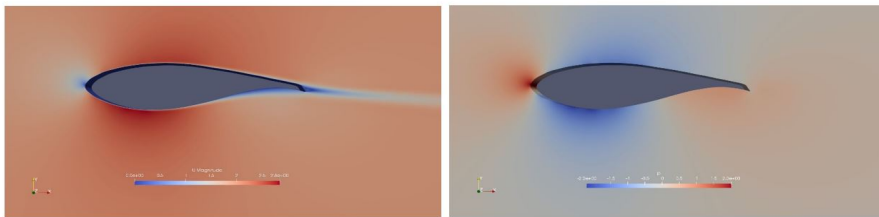
Figure 6.13: MHKF1-240s at -4 degree flow Angle (with velocity plot on the left and pressure plot on the right)

Although the shape of the foil has changed, the same observation can be reported in the MHKF1-240s at 0 degrees angle of flow, as an increase in pressure distribution towards the trailing edge on the lower side of the foil is observed with a corresponding decrease in velocity distribution. The pressure distribution decreases with an increasing velocity distribution even though a high pressure but low velocity is generated at the leading edge.
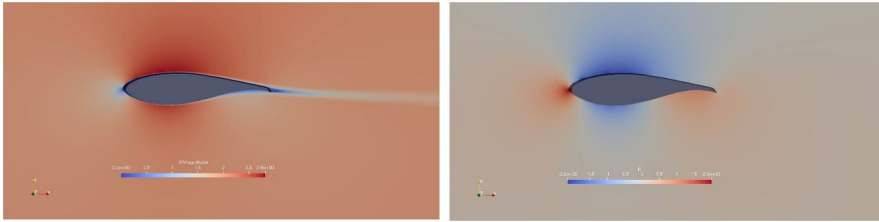
Figure 6.14: MHKF1-240s at 0 degree flow Angle (with velocity plot on the left and pressure plot on the right)

Fig 6.15 displays the simulation analysis result on the foil at an angle of 0 degree. A decreasing pressure distribution with an increasing velocity distribution can be observed. This brings about deceleration in pressure distribution and acceleration of the velocity distribution, the pressure however accelerates towards the trailing edge as there is no other force to stabilize the distribution with a deceleration in the velocity distribution.
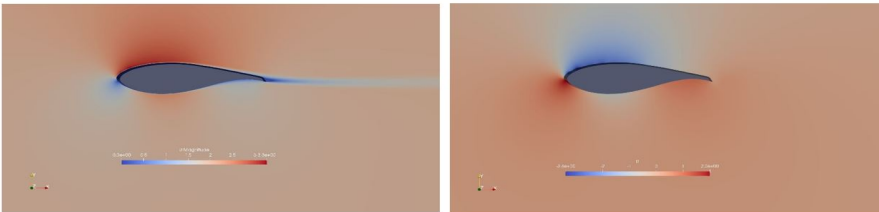
Figure 6.15: MHKF1-240s at 4 degrees flow Angle (with velocity plot on the left and pressure plot on the right)

With flow angle of 4 degrees, a slight increase in pressure flow can be observed at the mid part at the lower surface of the foil when compared with flow at an angle 0 degree. The pressure flow increases slightly also on the upper and increases more on the lower surface of the foil towards the trailing edge. However, the velocity distribution can be observed to decrease more towards the trailing edge on the lower surface of the foil than the upper surface.
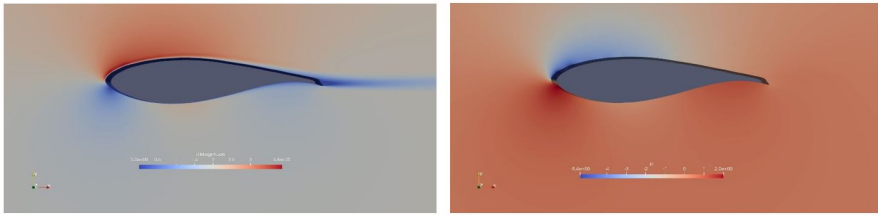
Figure 6.16: MHKF1-240s at 8 degrees flow Angle (with velocity plot on the left and pressure plot on the right)

At 8 degrees flow angle, it can be observed that the velocity flow over the upper and lower surface of the foil is decelerating towards the trailing edge, while the pressure distribution above the foil shows an increasing flow towards the trailing edge and a slight deceleration at the mid part of the foil on the lower surface, then increasing more towards the trailing edge.
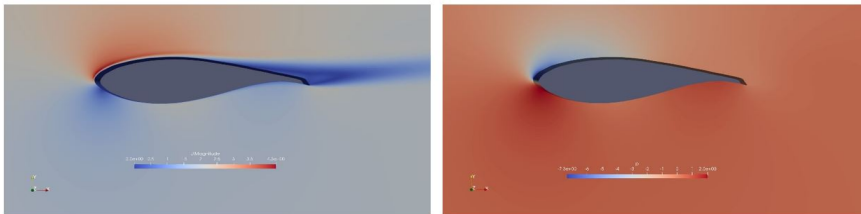
Figure 6.17: MHKF1-240s at 12 degrees flow Angle (with velocity plot on the left and pressure plot on the right)

As the the stagnation point moves more towards the lower surface, an early separation in the velocity distribution and also decrease towards the trailing edge of the foil is observed on the upper surface of the foil. However, increase in the velocity and pressure distribution can also be observed with an increase in pressure distribution on the upper surface of the foil.
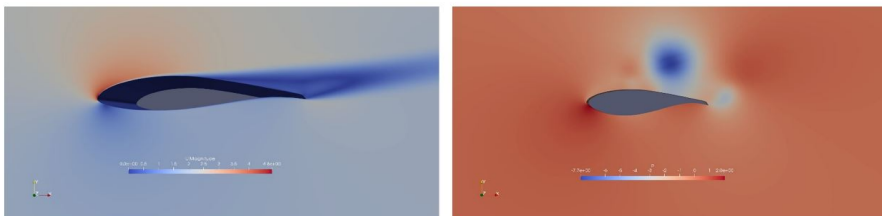
Figure 6.18: MHKF1-240s at 16 degrees flow Angle (with velocity plot on the left and pressure plot on the right)

Fig 6.19 displays the simulation analysis at a flow angle of 16 degrees. It can be observed at the trailing edge of upper surface of the foil that the pressure distribution decelerates which result in the wake noticed there, however, an increased pressure distribution is observed at the lower surface of the foil. The velocity distribution experience an early separation and decreases towards the trailing edge with a slightly increasing velocity distribution at the lower surface.
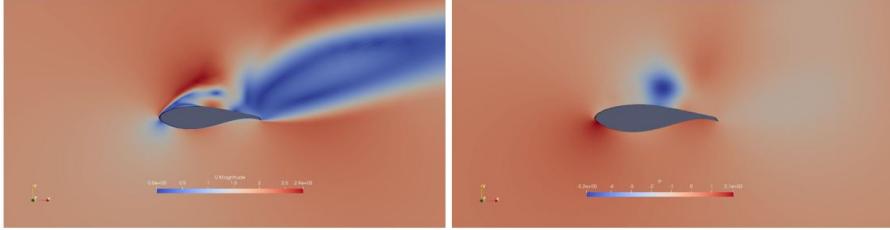
Figure 6.19: MHKF1-240s at 20 degrees flow Angle (with velocity plot on the left and pressure plot on the right)

This shows the simulation analysis of an extreme flow angle of 20 degrees in which the velocity distribution illustrates a very unstable flow over the upper surface of the foil and a large wake at the trailing edge as the flow is coming from under. As a result of the extreme angle of attack and an early flow separation point at the leading edge, the velocity distribution decelerated at the leading edge and a swirl-like flow can be observed at the mid part of the foil. The pressure flow at the lower surface however is much higher at the leading edge, decreases at the mid part of the foil and then accelerates towards the trailing edge.
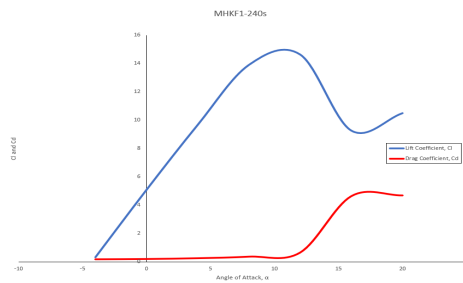
Figure 6.20: Lift and Drag Coefficient against Angle of Attack

The optimal angle of attack of the foil MHKF1-240s falls on 11.5 degrees as higher angle of attacks has higher drag than lift. As seen in Fig 6.20, even at low angle of attack, lift is already being generated. It is important to also note that this is the foil in the middle section of the turbine blade.

### 6.2.3 CFD simulation analysis of MHKF1-400 at varying angle of attack
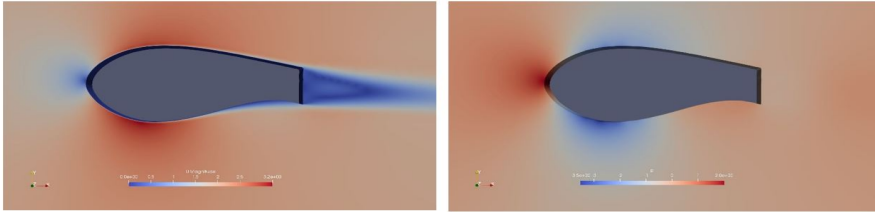
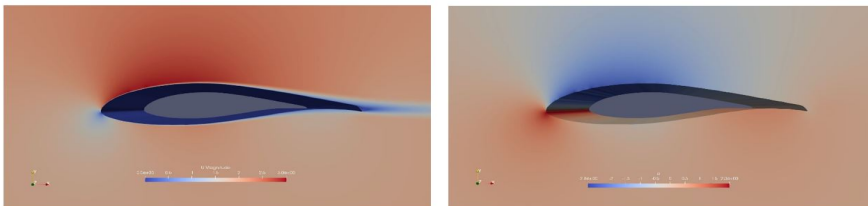**Figure 6.21:** MHKF1-400 at -4 degree flow Angle (with velocity plot on the left and pressure plot on the right)

At a flow angle of -4 degree, the pressure is almost the same at mid part of the upper and lower surface of the blade. The velocity distribution however decreases towards the trailing edge on the upper and lower surface creating wake as a result of the flat back at the trailing edge of the foil. Although, with a much lower pressure flow over the foil, the lower surface experiences a an increasing pressure flow than the upper surface of the foil.
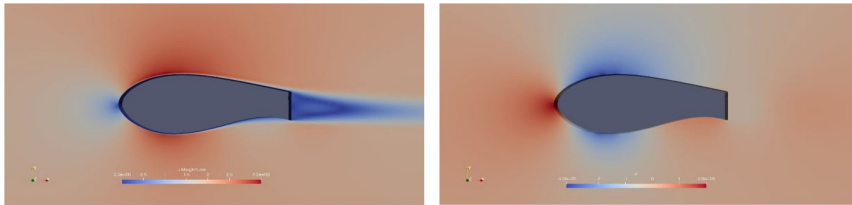
Figure 6.22: MHKF1-240s at 0 degree flow Angle (with velocity plot on the left and pressure plot on the right)

Analyzing the flow over the MHKF1-400 foil at a flow angle of 0 degree, a high velocity flow can be seen on the upper surface of the foil with a low velocity flow at the lower part which nicely converged at the trailing edge of the foil. The pressure flow displays a much higher flow at the lower surface of the foil while the flow over the upper surface is much lower. Viscous boundary layer can be seen as the flow has a high turbulence.
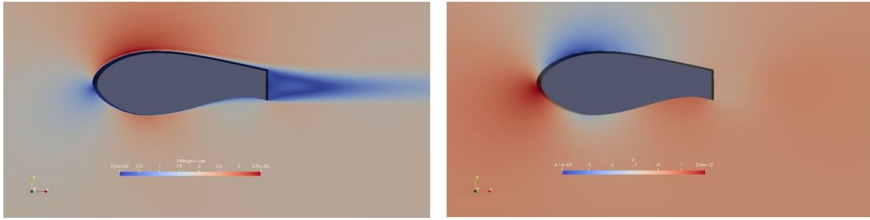
Figure 6.23: MHKF1-400 at 4 degree flow Angle (with velocity plot on the left and pressure plot on the right)

The flow dynamics can be observed at 4 degree flow angle over the foil with a high and low velocity flow at the upper and lower surface respectively. Meanwhile, the pressure flow shows a increasing pressure distribution at the lower surface and a more low pressure distribution at the upper surface.
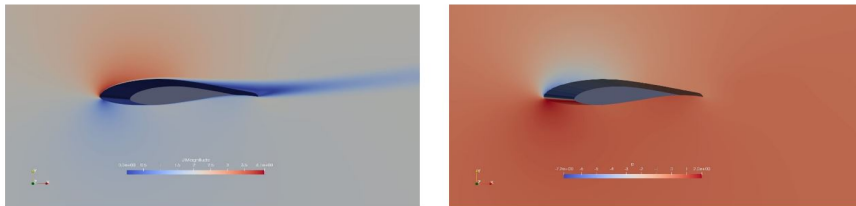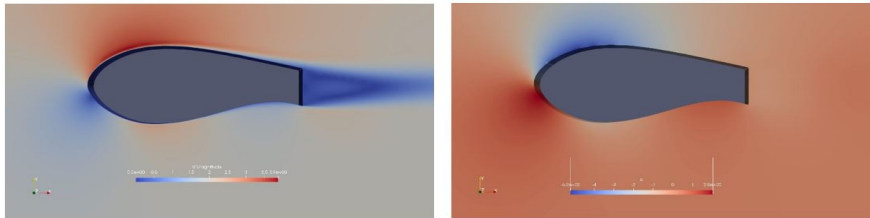

Figure 6.24: MHKF1-400 at 8 degree flow Angle (with velocity plot on the left and pressure plot on the right)

At flow angle of 8 degrees, the separation between the velocity flow and the foil starts as the viscous layer in between the flow and the the foil surface becomes visible with a decreasing velocity flow immediately on the upper surface of the foil. It can be observed that the pressure distribution is lower on the upper surface than the lower surface of the foil.
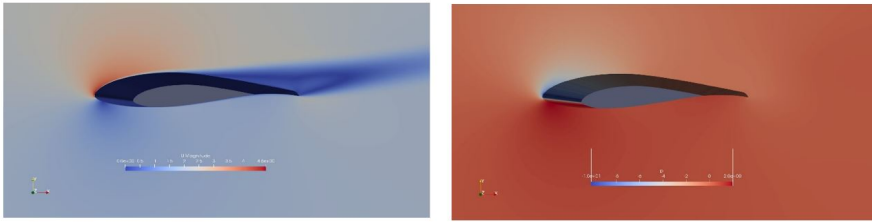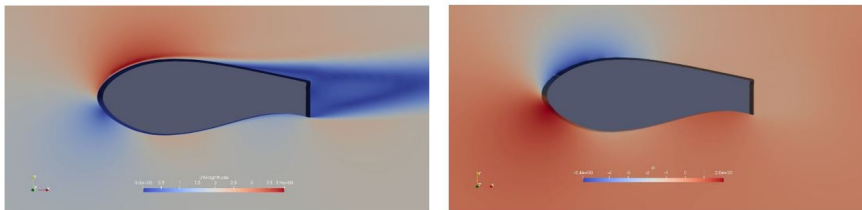

Figure 6.25: MHKF1-400 at 12 degree flow Angle (with velocity plot on the left and pressure plot on the right)

From the observation of the velocity flow at flow angle of 12 degrees over the

foil, the separation of flow which also started early results in a turbulent flow at the trailing edge of the foil and has a low velocity at the lower surface except a slight increase at the mid part. Meanwhile, a low pressure is experienced at the upper surface of the foil while the lower surface displays a high pressure flow.
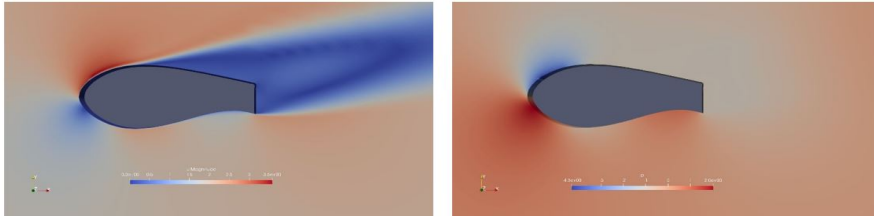
Figure 6.26: MHKF1-400 at 16 degrees flow Angle (with velocity plot on the left and pressure plot on the right)

At 16 degrees flow angle, an early separation point of flow can be seen with a high velocity flow at the leading edge on the upper surface and low velocity flow at the lower surface. The trailing edge of the velocity flow can be seen to have a high turbulent flow which can be attributed to be as a result of the increased flow angle. The pressure flow displays a low pressure gradient at the upper surface with a low pressure flow at the lower surface.
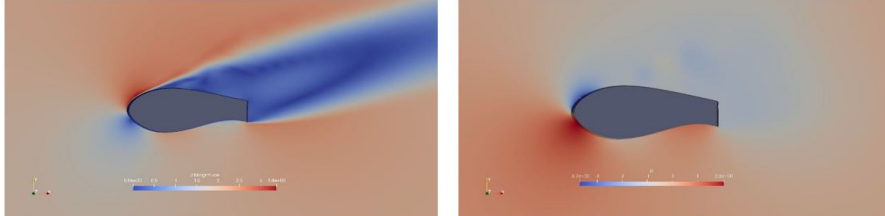
Figure 6.27: MHKF1-400 at 20 degrees flow Angle (with velocity plot on the left and pressure plot on the right)

This is expected at an extreme angle of 20 degrees over a flat back foil. The high velocity flow separates early at the leading edge resulting in rapid flow of turbulence towards the trailing edge while a low velocity flow can be observed over the lower surface of the foil. Meanwhile, taking a closer examination at the upper surface of the pressure, it can be observed to show some kind of turbulence even though not too obvious probably due to the high flow angle going over the foil. A low pressure flow can be observed at the leading edge before its early separation while the lower surface experiences a higher pressure.

After the simulation analysis, Fig 6.28 displays the Drag and Lift coefficient in relation to the varying angles of attack. An optimal Angle of attack is observed at 10 degrees as lift coefficient at higher angle begins to drop. It is however important to note that this is the foil at the root of the blade.
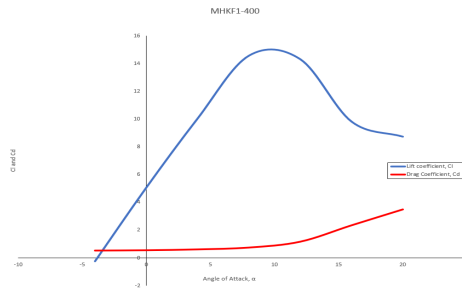
Figure 6.28: Lift and Drag Coefficient against Angle of Attack

6.2.4 BEMT validation result

Figure 6.29 displays the plot of the validation case of the 3-bladed turbine [6] which is also inline with BEM calculation yields a power coefficient of 0.45 at TSR of 4 at incoming velocity of 5m/s.
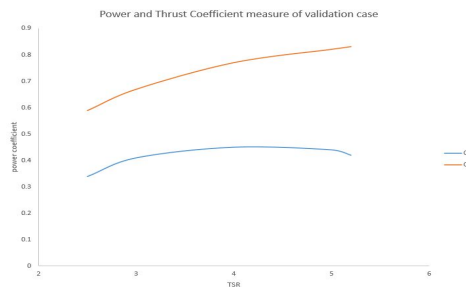
Figure 6.29: Validation case Blade loading and powering data inline with BEM calculations [6]

The BEMT generated power coeficient at TSR of 4 yiels an efficiency of 0.4, a little lower than the efficiency generated in the validation case [6].
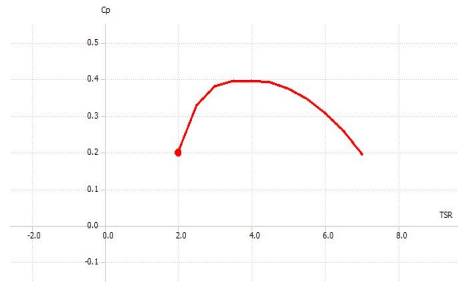
Figure 6.30: Power coefficient BEMT generated plot
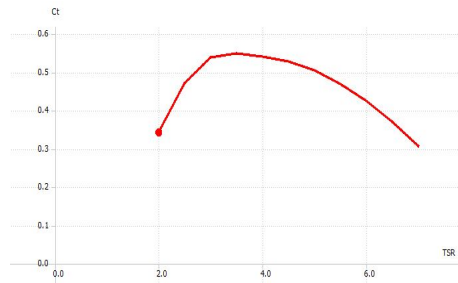
Figure 6.31: Thrust coefficient BEMT generated plot

Chapter 7

Conclusion

In this report the performance of a propeller was predicted using BEMT technique and the importance of this theory in the comprehension of an efficient propeller blade in relation to increasing incoming flow velocity on the propeller. Also, the generation of torque in order to derive the power coefficient or efficiency of the turbine as a whole was investigated.

Although the momentum theory comes in handy for theoretical study justification, however, when it comes to designing a propeller blade, the combination with the blade element theory brings about the BEMT (blade element momentum theory) which is a technique that has become employable in the analysis and design of propellers.

The CFD analysis of the Tidal turbine was performed and to conclude on the analysis of the Framo propeller in free stream, the pitch of the blades should probably be reduced towards the root and that would give an overall more optimal flow, but at a higher TSR. Also, it has been shown that the maximum Cp here is 0.28, which is not a great result but not terrible either.

As the COVID-19 situation rages more than anticipated, carrying out the research work from home was the only viable option and other challenges faced with access to useful softwares and computational space, resulting in a limited time to run the final simulations for the Ducted turbines.

7.1 Sources of error

OpenFoam showed it is a very effective tool for a comprehensive CFD simulation analysis of hydro propellers and at all stages of the design process, however, snappyHexMesh as a meshing tool in openFoam tends to be challenging in regard to generating fine meshes around the geometry. The mesh obtained from snappyHexMesh was not at all perfect and this can be traced back to a couple of errors generated during the course of meshing the model which are:

1. Non-orthogonality angle, which is the angle between two cell centres and the normal vector of the face is probably one source of error.

2. Skewness also can be a probable cause for the low quality mesh and this can be described as how far the angles of a cell deviate from a right angle, which is literally the sudden change in size of some cells can also be attributed to be another source of error generated from meshing.

7.2 Recommendation for future work

The aim of this research work was to analyze the effect of introducing a duct to a turbine and investigate the efficiency result in relation to a turbine without duct. However, only the analysis of the Framo AS propeller without duct, the BEM designed MHKF turbine blade and the analysis of each of the three foils that makes the long span blade could be achieved as a result of available time to run the simulation analysis. Therefore, the following recommendation for further improvement and research is proposed.

1. The Framo AS turbine blade pitch should be reduced towards the root in order to generate more optimal flow.

2. Mesh with a better meshing tool in order to obtain better mesh quality, thereby achieving reliable results.

3. Finally, the Ducted turbine analysis for both low and high solidity turbine is recommended future research.

Bibliography

[1] The wind tunnel fluid measurements e80 spring 2014.

[2] All about circuits. Torque conversion calculator.

[3] Mechanical Mechatronic Engg. University of Sydney Aerospace. Classification of flows, laminar and turbulent flows, 2005.

[4] M. R. Ahmed. Blade sections for different turbine and tidal current turbine applications-current status and future challenges. *International Journal of Energy Research*, 36(7):829–844, 2012.

[5] IIT Bombay Alumni. Boundary layer basics.

[6] A. Richard S. Arnold, A. William and L. Michael. A 1:8.7 scale water tunnel verification validation test of an axial flow water turbine. *The Pennsylvania State University APPLIED RESEARCH LABORATORY*, (10):2–5, August 2013.

[7] LEAP Australia. Tips tricks: Turbulence part 2 - wall functions and y+ requirements, 2019.

[8] J. Michael H. Bahram, H. Christian. *OpenFOAM® Basic Training*. Technische Universität Wien Institute of Chemical, Environmental and Bioscience Engineering, 4th edition, 2018.

[9] Belloni C. Hydrodynamics of ducted and open-centre tidal turbines. pages 127–129, 2013.

[10] B. I. Celik. *Introductory Turbulence Modeling Lectures Notes*. West Virginia University Mechanical Aerospace Engineering Dept., 1999.

[11] R. Chabay and B. Sherwood. *Matter Interactions II: Electric and Magnetic Interactions*. John Wiley and Sons, Inc., 3rd ed., 2009.

[12] D. Georgiou I.Hanegan K. C. Li-San H.Kulp M. Maygarden D.Retchless D. Cornell, S.Fitzgerald and B. Yarnal. Spring and neap tides, 2019.

[13] A. P. Dendy, S. Ketut and Mukhtasor. The influence of time step setting on the cfd simulation result of vertical axis tidal current turbine. *Journal of Mechanical Engineering and Sciences*, 12(1):3399–3401, 2018.

[14] R.G.J. Flay D.G. Phillips, P.J. Richards. Diffuser development for a diffuser augmented wind turbine using computational fluid dynamics. page 2, 2005.

[15] H. J. Fleming, C. F. Willden. Analysis of bi-directional ducted tidal turbine performance. *International Journal of Marine Energy*, pages 2–13, 2016.

[16] K. E. Giljarhus. Cfd simulations of a tidal turbine in a bi-directional duct. *University of Stavanger*, page 2, 2020.

[17] C. J. Greenshields. *The OpenFOAM Foundation: User Guide version 7*. OpenFOAM Foundation Ltd, 2019.

[18] M. D. Hossain. Power generation using tidal energy by artificial floating dam without turbine. pages 1–3, 2009.

[19] IEA. The oil and gas industry in energy transitions, iea, paris, 2020.

[20] S. M. Jamal. *Fluid Flow Handbook*. McGraw-Hill, 2002.

[21] M. Kenneth. *The ParaView Tutorial*. Sandia National Laboratories.

[22] Y. Azreen E. Nurhaslinda-K. Koh, K. K. Omar. The study of ducted propeller in propulsion performance of a malaysia fishing boat. *Jurnal Teknologi*, pages 39–43, 2015.

[23] K. Mansoor. Cardiovascular physiology. 2019.

[24] D. Marten. Qblade v0.01 guidelines. page 4, 2010.

[25] J. Pechlivanoglou G. Nayeri C. N. Paschereit C. O. Marten, D. Wendler. Qblade: An open source tool for design and simulation of horizontal and vertical axis wind turbines. *International Journal of Emerging Technology and Advanced Engineering*, 3(3):264–269, 2013.

[26] P. McLaren-Gow, S. Jamieson and J. M. R. Graham. A comparison between ducted turbine theory and inviscid simulation. pages 1–4, 2013.

[27] P. Moriarty and A. Hansen. *AeroDyn Theory Manual, Technical report*. National Renewable Energy Laboratory, 2005.

[28] United Nations. World population prospects 2019: Highlights. 2019.

[29] Ministry of Foreign Affairs of Denmark. Green thinking: Pioneers in clean energy, 2020.

[30] A. Owen. The application of low aspect ratio hydrofoils to the secure positioning of static equipment in tidal streams. 2007.

[31] M L. Owen, A. Trevor. Tidal current energy: origins and challenges. "future energy: improved, sustainable and clean options for our planet". 2008.

[32] L. Rainald. Applied cfd techniques: An introduction based on finite element methods. 2001.

[33] S. A. Robert. Possible roman tide mill. 2002.

[34] F. Reynolds A. Rourke, F. O. Boyle. Tidal energy update 2009. page 399, 2009.

[35] Q. Ruqiong and D. Chunyi. The principle and applications of bernoulli equation. *IOP Conf. Series: Journal of Physics: Conf. Series 916 (2017) 012038*, page 1, 2017.

[36] I. Sadrehaghighi. Turbulence modeling: A review. 2018.

[37] M. R. Shives. Hydrodynamic modeling, optimization and performance assessment for ducted and non-ducted tidal turbines. *University of Victoria*, 2008.

[38] P. N. Simon and M. H. Reza. *Fundamentals of Ocean Renewable Energy: Generating Electricity from the Sea*. Academic Press, 2018.

[39] P. N. Simon and M. H. Reza. *Fundamentals of Ocean Renewable Energy: Generating Electricity from the Sea*. Academic Press, 2018.

[40] Team Udvavisk. Significance of courant number for stability and convergence of cfd simulations, 2019.

[41] G. A. Veeksha, R. P. Kumar. Design and simulation of small wind turbine blades in q-blade. *International Journal of Engineering Development and Research, IJEDR*, 5(4):1099–1100, 2017.

[42] H. Winarto. Bemt algorithm for the prediction of the performance of arbitrary propellers. *International Journal of Emerging Technology and Advanced Engineering*, 3(1):4–8, 2004.

[43] I. A. Holt J. Burrows R. Wolf, J. Walkington. Environmental impacts of tidal power schemes. *Maritime Engineering*, 2014.

[44] J. M. Çengel, Y. A. Cimbala. *Fluid Mechanics: Fundamentals and Application. Third Edition*. McGraw Hill, 2014.

Appendix

Recall, force is a vector (with magnitude and direction).

Therefore,

Net force = vector sum of (pressure force and viscous force)

Thrust force (x-direction) = Pressure force + viscous force Torque = Pressure force +Viscous force

$$Drag force = F_{px} + F_{vx} \tag{7.1}$$

$$Lift force = F_{py} + F_{vy} \tag{7.2}$$

$$Reynolds number, Re = \frac{\rho v D}{u} \tag{7.3}$$

where u is the dynamic viscosity

$$yPlus, y+ = \frac{Uy}{v} = \frac{friction velocity * distance from wall}{kinematic viscosity} \tag{7.4}$$

$$C_f = \frac{0.026}{Re^0.143} \tag{7.5}$$

$$shear stress rate, \tau_w = \frac{C_f \rho U_y^2}{2} \tag{7.6}$$

$$Frictional velocity, U_f = \sqrt{\frac{\tau_w}{\rho}} \tag{7.7}$$

$$\Delta S = \frac{yPlus * u}{U_f \rho} \tag{7.8}$$

where u is the dynamic viscosity

In order to calculate the Lift and Drag direction of flow,

Lift direction, L = $f_y \cos(\alpha)$ - $f_x \sin(\alpha)$

Drag direction, D = $f_x \cos(\alpha)$ - $f_y \sin(\alpha)$

$$L = \frac{L}{\frac{1}{2}\rho A_p} \tag{7.9}$$

$$D = \frac{D}{\rho A \frac{v^2}{2}} \tag{7.10}$$

In the simulation analysis of the MHKF hydrofoils 180s, 240s and 400, Fig 7.1 shows the generated Drag and Lift at different angle of attacks.

```
/*--------------------------------*- C++ -*----------------------------------*\
| =========                 |                                                 |
| \\      /  F ield         | OpenFOAM: The Open Source CFD Toolbox           |
|  \\    /   O peration     | Website:  https://openfoam.org                  |
|   \\  /    A nd           | Version:  dev                                   |
|    \\/     M anipulation  |                                                 |
\*---------------------------------------------------------------------------*/
FoamFile
{
    version     2.0;
    format      ascii;
    class       volVectorField;
    location    "0";
    object      U;
}
// * * * * * * * * * * * * * * * * * * * * * * * * * * * * * * * * * * * * * //

dimensions      [0 1 -1 0 0 0 0];

internalField   uniform (2 0 0);

boundaryField
{
    airfoil
    {
        type            fixedValue;
        value           uniform (0 0 0);
    }
    back
    {
        type            empty;
    }
    farfield
    {
        type            freestream;
        freestreamValue uniform (2 0 0);
        value           uniform (2 0 0);
    }
    front
    {
        type            empty;
    }
}

// ************************************************************************* //
```

```
/*--------------------------------*- C++ -*----------------------------------*\
| =========                 |                                                 |
| \\      /  F ield         | OpenFOAM: The Open Source CFD Toolbox           |
|  \\    /   O peration     | Website:  https://openfoam.org                  |
|   \\  /    A nd           | Version:  dev                                   |
|    \\/     M anipulation  |                                                 |
\*---------------------------------------------------------------------------*/
FoamFile
{
    version     2.0;
    format      ascii;
    class       volScalarField;
    location    "0";
    object      p;
}
// * * * * * * * * * * * * * * * * * * * * * * * * * * * * * * * * * * * * * //

dimensions      [0 2 -2 0 0 0 0];

internalField   uniform 0;

boundaryField
{
    airfoil
    {
        type            zeroGradient;
    }
    back
    {
        type            empty;
    }
    farfield
    {
        type            freestreamPressure;
        freestreamValue uniform 0;
        supersonic      false;
        value           uniform 0;
    }
    front
    {
        type            empty;
    }
}

// ************************************************************************* //
```

```
/*--------------------------------*- C++ -*----------------------------------*\
| =========                 |                                                 |
| \\      /  F ield         | OpenFOAM: The Open Source CFD Toolbox           |
|  \\    /   O peration     | Website:  https://openfoam.org                  |
|   \\  /    A nd           | Version:  dev                                   |
|    \\/     M anipulation  |                                                 |
\*---------------------------------------------------------------------------*/
FoamFile
{
    version     2.0;
    format      ascii;
    class       volScalarField;
    location    "0";
    object      nuTilda;
}
// * * * * * * * * * * * * * * * * * * * * * * * * * * * * * * * * * * * * * //

dimensions      [0 2 -1 0 0 0 0];

internalField   uniform 7.5e-05;

boundaryField
{
    airfoil
    {
        type            fixedValue;
        value           uniform 0;
    }
    back
    {
        type            empty;
    }
    farfield
    {
        type            freestream;
        freestreamValue uniform 7.5e-05;
        value           uniform 7.5e-05;
    }
    front
    {
        type            empty;
    }
}

// ************************************************************************* //
```

```
/*--------------------------------*- C++ -*----------------------------------*\
| =========                 |                                                 |
| \\      /  F ield         | OpenFOAM: The Open Source CFD Toolbox           |
|  \\    /   O peration     | Website:  https://openfoam.org                  |
|   \\  /    A nd           | Version:  dev                                   |
|    \\/     M anipulation  |                                                 |
\*---------------------------------------------------------------------------*/
FoamFile
{
    version     2.0;
    format      ascii;
    class       volScalarField;
    location    "0";
    object      nut;
}
// * * * * * * * * * * * * * * * * * * * * * * * * * * * * * * * * * * * * * //

dimensions      [0 2 -1 0 0 0 0];

internalField   uniform 1.94e-05;

boundaryField
{
    airfoil
    {
        type            nutUSpaldingWallFunction;
        Cmu             0.09;
        kappa           0.41;
        E               9.8;
        value           uniform 0;
    }
    back
    {
        type            empty;
    }
    farfield
    {
        type            freestream;
        freestreamValue uniform 1.94e-05;
        value           uniform 1.94e-05;
    }
    front
    {
        type            empty;
    }
}

// ************************************************************************* //
```

```
/*--------------------------------*- C++ -*----------------------------------*\
| =========                 |                                                 |
| \\      /  F ield         | OpenFOAM: The Open Source CFD Toolbox           |
|  \\    /   O peration     | Version: 2.0.0                                  |
|   \\  /    A nd           | Web:     www.OpenFOAM.com                       |
|    \\/     M anipulation  |                                                 |
\*---------------------------------------------------------------------------*/
FoamFile
{
    version     2.0;
    format      ascii;
    class       dictionary;
    object      controlDict;
}
// * * * * * * * * * * * * * * * * * * * * * * * * * * * * * * * * * * * * * //

application     simpleFoam;

startFrom       latestTime;

startTime       0;

stopAt          endTime;

endTime         6000;

deltaT          1;

writeControl    timeStep;

writeInterval   1000;

purgeWrite      0;

writeFormat     ascii;

writePrecision  6;

writeCompression uncompressed;

timeFormat      general;

timePrecision   6;

runTimeModifiable true;

libs
(
);

functions
{
    #include "forceCoeffs"
    #include "yPlus"
}

// *************************************************************************** //
```

```
/*--------------------------------*- C++ -*----------------------------------*\
| =========                 |                                                 |
| \\      /  F ield         | OpenFOAM: The Open Source CFD Toolbox           |
|  \\    /   O peration     | Version: 2.1.x                                  |
|   \\  /    A nd           | Web:     www.OpenFOAM.org                       |
|    \\/     M anipulation  |                                                 |
\*---------------------------------------------------------------------------*/
FoamFile
{
    version     2.0;
    format      ascii;
    class       dictionary;
    location    "system";
    object      fvSchemes;
}
// * * * * * * * * * * * * * * * * * * * * * * * * * * * * * * * * * * * * * //

ddtSchemes
{
    default         steadyState;
}

gradSchemes
{
    default         Gauss linear;
}

divSchemes
{
    default         none;
    div(phi,U)      Gauss linearUpwind grad(U);
    div(phi,nuTilda) Gauss upwind;
    div((nuEff*dev2(T(grad(U))))) Gauss linear;
}

laplacianSchemes
{
    default         Gauss linear corrected;
}

intepolationSchemes
{
    default         linear;
}

snGradSchemes
{
    default         corrected;
}

fluxRequired
{
    default         no;
    p;
}

wallDist
{
    method meshWave;
}

// *************************************************************************** //
```

```
/*--------------------------------*- C++ -*----------------------------------*\
| =========                 |                                                 |
| \\      /  F ield         | OpenFOAM: The Open Source CFD Toolbox           |
|  \\    /   O peration     | Version:  2.1.x                                 |
|   \\  /    A nd           | Web:      www.OpenFOAM.org                      |
|    \\/     M anipulation  |                                                 |
\*---------------------------------------------------------------------------*/
FoamFile
{
    version     2.0;
    format      ascii;
    class       dictionary;
    location    "system";
    object      fvSolution;
}
// * * * * * * * * * * * * * * * * * * * * * * * * * * * * * * * * * * * * * * //

solvers
{
    p
    {
        solver          GAMG;
        tolerance       1e-06;
        relTol          0.001;
        smoother        GaussSeidel;
    }
Phi
{
$p;
}
    U
    {
        solver          smoothSolver;
        smoother        GaussSeidel;
        nSweeps         2;
        tolerance       1e-08;
        relTol          0.01;
    }
    nuTilda
    {
        solver          smoothSolver;
        smoother        GaussSeidel;
        nSweeps         2;
        tolerance       1e-08;
        relTol          0.1;
    }
}

SIMPLE
{
    nNonOrthogonalCorrectors 1;
    pRefCell        0;
    pRefValue       0;
}
potentialFlow
{
    nNonOrthogonalCorrectors 10;
}
relaxationFactors
{
    fields
    {
        p           0.3;
    }
    equations
    {
        U           0.7;
        nuTilda     0.7;
    }
}


// ************************************************************************* //
```

```
/*--------------------------------*- C++ -*----------------------------------*\
| \\      / F ield         | OpenFOAM: The Open Source CFD Toolbox           |
|  \\    /  O peration     | Version:  2.1.x                                 |
|   \\  /   A nd           | Web:      www.OpenFOAM.org                      |
|    \\/    M anipulation  |                                                |
\*---------------------------------------------------------------------------*/
FoamFile
{
    version     2.0;
    format      ascii;
    class       dictionary;
    location    "system";
    object      fvSchemes;
}
// * * * * * * * * * * * * * * * * * * * * * * * * * * * * * * * * * * * * * //

ddtSchemes
{
    default         steadyState;
}

gradSchemes
{
    default         Gauss linear;
}
divSchemes
{
    default           none;
    div(phi,U)        Gauss linearUpwind grad(U);
    div(phi,nuTilda)  Gauss upwind;
    div((nuEff*dev2(T(grad(U))))) Gauss linear;
}

laplacianSchemes
{
    default         Gauss linear corrected;
}
interpolationSchemes
{

    default       linear;
}

snGradSchemes
{
    default         corrected;
}

fluxRequired
{
    default         no;
    p;
}
wallDist
{
    method meshWave;
}
// ************************************************************************* //
```

□

For the framo AS propeller simulation analysis, the openFoam scripts used are pasted below;

```
/*--------------------------------*- C++ -*----------------------------------*\
  =========                 |
  \\      /  F ield         | OpenFOAM: The Open Source CFD Toolbox
   \\    /   O peration     | Website:  https://openfoam.org
    \\  /    A nd           | Version:  dev
     \\/     M anipulation  |
\*---------------------------------------------------------------------------*/
FoamFile
{
    version     2.0;
    format      binary;
    class       volVectorField;
    location    "0";
    object      U;
}
// * * * * * * * * * * * * * * * * * * * * * * * * * * * * * * * * * * * * * //

dimensions      [0 1 -1 0 0 0 0];

internalField   uniform (2.54 0 0);

boundaryField
{
    #includeEtc "caseDicts/setConstraintTypes"
    walls
    {
        type            slip;
    }
    inlet
    {
        type            fixedValue;
        value           uniform (2.54 0 0);
    }
    outlet
    {
        type            inletOutlet;
        inletValue      uniform (0 0 0);
        value           uniform (0 0 0);
    }
    hub
    {
        type            movingWallVelocity;
        value           uniform (0 0 0);
    }
    propeller
    {
        type            movingWallVelocity;
        value           uniform (0 0 0);
    }
}


// ************************************************************************* //
```

```
/*--------------------------------*- C++ -*----------------------------------*\
  =========                 |
  \\      /  F ield         | OpenFOAM: The Open Source CFD Toolbox
   \\    /   O peration     | Website:  https://openfoam.org
    \\  /    A nd           | Version:  dev
     \\/     M anipulation  |
\*---------------------------------------------------------------------------*/
FoamFile
{
    version     2.0;
    format      ascii;
    class       volScalarField;
    location    "0";
    object      p;
}
// * * * * * * * * * * * * * * * * * * * * * * * * * * * * * * * * * * * * * //

dimensions      [0 2 -2 0 0 0 0];

internalField   uniform 0;

boundaryField
{
    //- Set patchGroups for constraint patches
    #includeEtc "caseDicts/setConstraintTypes"

    inlet
    {
        type            zeroGradient;
    }

    outlet
    {
        type            fixedValue;
        value           uniform 0;
    }

    wall
    {
        type            zeroGradient;
    }
    walls
    {
        type            slip;
    }
}


// ************************************************************************* //
```

```
/*--------------------------------*- C++ -*----------------------------------*\
| =========                 |                                                 |
| \\      /  F ield         | OpenFOAM: The Open Source CFD Toolbox           |
|  \\    /   O peration     | Version:  4.0                                   |
|   \\  /    A nd           | Web:      www.OpenFOAM.org                      |
|    \\/     M anipulation  |                                                 |
\*---------------------------------------------------------------------------*/
FoamFile
{
    version     2.0;
    format      ascii;
    class       volScalarField;
    object      omega;
}
// * * * * * * * * * * * * * * * * * * * * * * * * * * * * * * * * * * * * * //


dimensions      [0 0 -1 0 0 0 0];

internalField   uniform 96.774;

boundaryField
{
    #includeEtc "caseDicts/setConstraintTypes"
    inlet
    {
        type            fixedValue;
        value           $internalField;
    }


    outlet
    {
        type            inletOutlet;
        inletValue      $internalField;
        value           $internalField;
    }

    sphere
    {
        type            omegaWallFunction;
        value           $internalField;
    }

    wall
    {
        type            omegaWallFunction;
        value           $internalField;
    }
    walls
    {
        type            slip;
    }

}


// ************************************************************************* //
```

```
/*--------------------------------*- C++ -*----------------------------------*\
  =========                 |
  \\      /  F ield         | OpenFOAM: The Open Source CFD Toolbox
   \\    /   O peration     | Website:  https://openfoam.org
    \\  /    A nd           | Version:  dev
     \\/     M anipulation  |
\*---------------------------------------------------------------------------*/
FoamFile
{
    version     2.0;
    format      ascii;
    class       volScalarField;
    location    "0";
    object      nut;
}
// * * * * * * * * * * * * * * * * * * * * * * * * * * * * * * * * * * * * * //

dimensions      [0 2 -1 0 0 0 0];

internalField   uniform 0;

boundaryField
{
    //- Set patchGroups for constraint patches
    #includeEtc "caseDicts/setConstraintTypes"

    inlet
    {
        type            calculated;
        value           uniform 0;
    }

    outlet
    {
        type            calculated;
        value           uniform 0;
    }

    wall
    {
        type            nutUSpaldingWallFunction;
        value           uniform 0;
    }
    walls
    {
        type            nutUSpaldingWallFunction;
        value           uniform 0;
    }
}


// ************************************************************************* //
```

```
/*--------------------------------*- C++ -*----------------------------------*\
  =========                 |
  \\      /  F ield         | OpenFOAM: The Open Source CFD Toolbox
   \\    /   O peration     | Website:  https://openfoam.org
    \\  /    A nd           | Version:  dev
     \\/     M anipulation  |
\*---------------------------------------------------------------------------*/
FoamFile
{
    version     2.0;
    format      ascii;
    class       volScalarField;
    location    "0";
    object      k;
}
// * * * * * * * * * * * * * * * * * * * * * * * * * * * * * * * * * * * * * * //

dimensions      [0 2 -2 0 0 0 0];

internalField   uniform 0.00096774;

boundaryField
{
    //- Set patchGroups for constraint patches
    #includeEtc "caseDicts/setConstraintTypes"

    inlet
    {
        type            fixedValue;
        value           $internalField;
    }

    outlet
    {
        type            inletOutlet;
        inletValue      $internalField;
        value           $internalField;
    }

    wall
    {
        type            kqRWallFunction;
        value           $internalField;
    }

    walls
    {
        type            slip;
    }
}


// ************************************************************************* //
```

```
/*--------------------------------*- C++ -*----------------------------------*\
  =========                 |
  \\      /  F ield         | OpenFOAM: The Open Source CFD Toolbox
   \\    /   O peration     | Website:  https://openfoam.org
    \\  /    A nd           | Version:  dev
     \\/     M anipulation  |
\*---------------------------------------------------------------------------*/
FoamFile
{
    version     2.0;
    format      ascii;
    class       dictionary;
    object      blockMeshDict;
}

// * * * * * * * * * * * * * * * * * * * * * * * * * * * * * * * * * * * * * //

convertToMeters 1.0;

vertices
(
    (-1.99 -2 -2)
    ( 8 -2 -2)
    ( 8  2.0 -2)
    (-1.99  2.0 -2)
    (-1.99 -2  2)
    ( 8 -2  2)
    ( 8  2.0  2)
    (-1.99  2.0  2)
);

blocks
(
    hex (0 1 2 3 4 5 6 7) (160 64 64) simpleGrading (1 1 1)
);

edges
(
);

boundary
(
    walls
    {
        type wall;
        faces
        (
            (1 5 4 0)
            (3 7 6 2)
            (4 5 6 7)
            (0 3 2 1)
        );
    }
    inlet
    {
        type patch;
        faces
        (
            (0 4 7 3)
        );
    }
    outlet
    {
        type patch;
        faces
        (
            (2 6 5 1)
        );
    }
);
```

```
/*--------------------------------*- C++ -*----------------------------------*\
  =========                 |
  \\      /  F ield         | OpenFOAM: The Open Source CFD Toolbox
   \\    /   O peration     | Website:  https://openfoam.org
    \\  /    A nd           | Version:  dev
     \\/     M anipulation  |
\*---------------------------------------------------------------------------*/
FoamFile
{
    version     2.0;
    format      ascii;
    class       dictionary;
    location    "system";
    object      controlDict;
}
// * * * * * * * * * * * * * * * * * * * * * * * * * * * * * * * * * * * * * //

application     pimpleFoam;

startFrom       latestTime;

startTime       0;

stopAt          endTime;

endTime         1.5;

//deltaT              0.0015;
//writeControl    adjustableRunTime;
//writeInterval   0.030;

////- For testing with moveDynamicMesh
deltaT          0.01;
writeControl    timeStep;
writeInterval   1;

purgeWrite      0;

writeFormat     binary;

writePrecision  6;

writeCompression off;

timeFormat      general;

timePrecision   6;

runTimeModifiable true;

adjustTimeStep  no;

maxCo           0.9;

functions
{
    #includeFunc Q
    #include "surfaces"
    #include "forces"
    #includeFunc residuals
    //#include "forceCoeffs"
    //#includeFunc flowRatePatch(name=outlet)
}

// ************************************************************************* //
```

```
/*--------------------------------*- C++ -*----------------------------------*\
  =========                 |
  \\      /  F ield         | OpenFOAM: The Open Source CFD Toolbox
   \\    /   O peration     | Website:  https://openfoam.org
    \\  /    A nd           | Version:  dev
     \\/     M anipulation  |
\*---------------------------------------------------------------------------*/
FoamFile
{
    version     2.0;
    format      ascii;
    class       dictionary;
    object      createPatchDict;
}

// * * * * * * * * * * * * * * * * * * * * * * * * * * * * * * * * * * * * * //

internalFacesOnly true;

baffles
{
    rotating
    {
        type      faceZone;
        zoneName  rotCylinder;

        patches
        {
            master
            {
                name          AMI1;
                type          cyclicAMI;
                neighbourPatch  AMI2;
                        lowWeightCorrection 0.2;
            }

            slave
            {
                name          AMI2;
                type          cyclicAMI;
                neighbourPatch  AMI1;
                        lowWeightCorrection 0.2;
            }
        }
    }
}


// ************************************************************************* //
```

```
/*--------------------------------*- C++ -*----------------------------------*\
  =========                 |
  \\      /  F ield         | OpenFOAM: The Open Source CFD Toolbox
   \\    /   O peration     | Website:  https://openfoam.org
    \\  /    A nd           | Version:  dev
     \\/     M anipulation  |
\*---------------------------------------------------------------------------*/
FoamFile
{
    version     2.0;
    format      ascii;
    class       dictionary;
    location    "system";
    object      fvSchemes;
}
// * * * * * * * * * * * * * * * * * * * * * * * * * * * * * * * * * * * * * //

ddtSchemes
{
    default        Euler;
}

gradSchemes
{
    default        Gauss linear;
    grad(p)        Gauss linear;
    grad(U)        cellLimited Gauss linear 1;
}

divSchemes
{
    default        none;
    //div(phi,U)      Gauss upwind;
    div(phi,U)      Gauss linearUpwind grad(U);
    div(phi,k)      Gauss upwind;
    div(phi,epsilon) Gauss upwind;
    div(phi,omega) Gauss upwind;
    div((nuEff*dev2(T(grad(U))))) Gauss linear;
    div(div(phi,U)) Gauss linear;
}

laplacianSchemes
{
    default        Gauss linear limited corrected 0.333;
}

interpolationSchemes
{
    default        linear;
}

snGradSchemes
{
    default        limited corrected 0.333;
}

    wallDist
    {
      method meshWave;
    }

// ************************************************************************* //
```

```
/*--------------------------------*- C++ -*----------------------------------*\
| =========                 |                                                 |
| \\      /  F ield         | OpenFOAM: The Open Source CFD Toolbox           |
|  \\    /   O peration     | Website:  https://openfoam.org                  |
|   \\  /    A nd           | Version:  dev                                   |
|    \\/     M anipulation  |                                                 |
\*---------------------------------------------------------------------------*/
FoamFile
{
    version     2.0;
    format      ascii;
    class       dictionary;
    object      fvSolution;
}
// * * * * * * * * * * * * * * * * * * * * * * * * * * * * * * * * * * * * * //

solvers
{
    p
    {
        solver          GAMG;
        smoother        GaussSeidel;
        cacheAgglomeration no;
        maxIter         100;
        tolerance       1e-6;
        relTol          0.01;
    }

    pFinal
    {
        $p;

        tolerance       1e-2;
        relTol          0;
    }

    "pcorr.*"
    {
        tolerance       1e-7;
        relTol          0;
    }

    "(U|k|omega)"
    {
        solver          smoothSolver;
        smoother        symGaussSeidel;

        tolerance       1e-7;
        relTol          0.1;
    }

    "(U|k|omega)Final"
    {
        solver          smoothSolver;
        smoother        symGaussSeidel;

        tolerance       1e-7;
        relTol          0;
    }

    Phi
    {
        solver GAMG;
        agglomerator faceAreaPair;
        mergeLevels 1;
        cacheAgglomeration true;
        nCellsInCoarsestLevel 200;
        tolerance 1e-7;
        relTol 0.01;
        smoother GaussSeidel;
        nPreSweeps 0;
        nPostSweeps 2;
        nFinestSweeps 2;
        minIter 1;
    }
}

potentialFlow
{
    nNonOrthogonalCorrectors 10;
}

PIMPLE
{
    consistent yes;
    nNonOrthogonalCorrectors 0;
    pRefCell        0;
    pRefValue       0;
}

/*
relaxationFactors
{
    fields
    {
        p               0.3;
    }
    equations
    {
        U               0.7;
        k               0.7;
        omega           0.7;
        omega           0.7;
    }
}
*/
```

```
PIMPLE
{
    consistent yes;
    correctPhi       yes;
    nOuterCorrectors    50;
    nCorrectors       2;
    nNonOrthogonalCorrectors 0;
    outerCorrectorResidualControl
    {
            "(U|k|omega|nuTilda|p)"
            {
                relTol 0;
                tolerance 0.001;
            }
    }
}

relaxationFactors
{
// "(U|k|omega|nuTilda).*"   1;

    fields
    {
        p     0.3;
        pFinal   1;
    }
    equations
    {
        "U|k|omega|nuTilda"     0.7;
        "(U|k|omega|nuTilda)Final"   1;
    }
}

cache
{
    grad(U);
}

// ************************************************************************* //
```

```
/*--------------------------------*- C++ -*----------------------------------*\
  =========                 |
  \\      /  F ield         | OpenFOAM: The Open Source CFD Toolbox
   \\    /   O peration     | Website:  https://openfoam.org
    \\  /    A nd           | Version:  dev
     \\/     M anipulation  |
\*---------------------------------------------------------------------------*/
FoamFile
{
    version     2.0;
    format      ascii;
    class       dictionary;
    object      snappyHexMeshDict;
}
// * * * * * * * * * * * * * * * * * * * * * * * * * * * * * * * * * * * * * //

castellatedMesh true;
snap            true;
addLayers       true;


geometry
{
    rotCylinder
    {
        type     triSurfaceMesh;
        file     "rotCyl.stl";
    }
    hub { type     triSurfaceMesh; file     "framo_propellerHub.stl"; }
    propeller { type     triSurfaceMesh; file     "framo_propeller.stl"; }

            refinementBox
    {
        type searchableBox;
        min (-0.4 -0.3 -0.3);
        max ( 0.8  0.3  0.3);
    }

};

castellatedMeshControls
{

    // Refinement parameters

    maxLocalCells 100000;
    maxGlobalCells 200000000;
    minRefinementCells 0;
    maxLoadUnbalance 0.10;
    nCellsBetweenLevels 8;

    // Surface based refinement


    refinementSurfaces
    {

        rotCylinder
        {
            level      (4 4);
            cellZone   rotCylinder;
            faceZone   rotCylinder;
            cellZoneInside  inside;


        }

        hub { level      (4 4); }

        propeller { level      (4 4); }
    }
```

```
    resolveFeatureAngle 30; //30;

  // Region-wise refinement

  refinementRegions
  {
    rotCylinder
    {
      mode      inside;
      levels    ((1E15 2));
    }

            refinementBox
    {
      mode inside;
      levels ((1E15 3));
    }
  }
  // Mesh selection
  locationInMesh (7.11 0.11 1.03);
  allowFreeStandingZoneFaces false;
}
snapControls
{
  nSmoothPatch 3
  tolerance 2.0;
  nSolveIter 100;

  nRelaxIter 5;

    nFeatureSnapIter 100;

    implicitFeatureSnap true;

    explicitFeatureSnap false;

    multiRegionFeatureSnap true;
}
addLayersControls
{
  relativeSizes true;
  layers
  {
          "(propeller).*"
    {
      nSurfaceLayers 3;
    }
  }
  expansionRatio 1.3;
  finalLayerThickness 0.3;
  minThickness 0.0001;
    nGrow 0;
  featureAngle 90;
  nRelaxIter 10;
  nSmoothSurfaceNormals 1;
  nSmoothNormals 3;
  nSmoothThickness 10;
  maxFaceThicknessRatio 0.9;
  maxThicknessToMedialRatio 0.9;
  minMedianAxisAngle 90;
  nBufferCellsNoExtrude 0;
  nLayerIter 100;
}
meshQualityControls
{
  #include "meshQualityDict"
}
mergeTolerance 1e-6;


// *************************************************************************** //
```

Table 7.1: Drag and Lift coefficient for hydrofoils 180s, 240s and 400 at varying Angle of Attack

MHKF1 Hydrofoils						
	180s		240s		400	
Drag and Lift Coefficients						
AoA	cd	cl	cd	cl	cd	cl
-4	0.0208	-0.025	0.1835	0.328	0.5419	-0.256
0	0.0215	-0.43	0.205	5.097	0.564	5.058
4	0.02	0.86	0.26	9.68	0.626	10.04
8	0.0368	1.238	0.3708	13.91	0.757	14.57
12	0.058	1.44	0.659	14.64	1.18	14.319
16	0.089	1.55	4.65	9.27	2.36	9.82
20	0.188	1.26	4.7018	10.5	3.507	8.73